THERMOMECHANICAL FATIGUE OF MAR-M247: EXTENSION OF A UNIFIED CONSTITUTIVE AND LIFE MODEL TO HIGHER TEMPERATURES

A Thesis
Presented to
The Academic Faculty

by

Kyle A. Brindley

In Partial Fulfillment
of the Requirements for the Degree
Master of Science in the
George W. Woodruff School of Mechanical Engineering

Georgia Institute of Technology
May 2014

THERMOMECHANICAL FATIGUE OF MAR-M247: EXTENSION OF A UNIFIED CONSTITUTIVE AND LIFE MODEL TO HIGHER TEMPERATURES

Approved by:

Dr. Richard W. Neu, Advisor
George W. Woodruff School of Mechanical Engineering
School of Materials Science and Engineering
Georgia Institute of Technology

Dr. David L. McDowell
George W. Woodruff School of Mechanical Engineering
School of Materials Science and Engineering
Georgia Institute of Technology

Dr. Olivier N. Pierron
George W. Woodruff School of Mechanical Engineering
Georgia Institute of Technology

Date Approved: March 24, 2014

ACKNOWLEDGEMENTS

The work presented in this thesis would not have been possible without the support and assistance of a number of people. Their support greatly improved the quality of this work and contributed to my development as a student and researcher. I would like to express my gratitude to these people.

I would like to thank my advisor, Dr. Richard W. Neu, for his guidance and support. His expertise and aid were critical in the completion of this thesis. It was a pleasure to work with him, and I have learned a great deal in the process. I would also like to thank my committee members, Dr. David McDowell and Dr. Olivier Pierron, for their assistance and insight in reviewing this thesis.

I would like to thank Patxi Fernandez-Zelaia and Mike Kirka for their efforts in running the experiments presented in this thesis. Without their help and advice, the completion of this work would have taken considerably longer.

I would also like to thank my friends and co-workers Sean Neal and Ashley Nelson for their support and advice regarding this research and research and graduate school in general.

I would also like to thank the sponsor of this research, Pratt & Whitney, particularly Dr. David Furrer and Shawn Gregg. Without the financial support, this research would not have been possible. I would like to thank the Pratt & Whitney technical point of contact for this work, Masamichi Hongoh. Additionally, I would like to thank Bessem Jlidi for his sound technical advice and support in the development of the codes required to implement the models.

Finally, I would like to thank my family for their encouragement and support throughout my academic career. I owe my work ethic and continued curiosity and

interest for science and engineering to the teaching and example of my parents. I would also like to thank my many friends who have encouraged me both academically and personally.

TABLE OF CONTENTS

LIST OF TABLES

LIST OF FIGURES

SUMMARY

The goal of this work is to establish a life prediction methodology for thermomechanical loading of the Ni-base superalloy Mar-M247 over a larger temperature range than previous work. The work presented in this thesis extends the predictive capability of the Sehitoglu-Boismier unified thermo-viscoplasticity constitutive model and thermomechanical life model from a maximum temperature of 871°C to a maximum temperature of 1038°C. The constitutive model, which is suitable for predicting stress-strain history under thermomechanical loading, is adapted and calibrated using the response from isothermal cyclic experiments conducted at temperatures from 500°C to 1038°C at different strain rates with and without dwells. In the constitutive model, the flow rule function and parameters as well as the temperature dependence of the evolution equation for kinematic hardening are established. In the elevated temperature regime, creep and stress relaxation are critical behaviors captured by the constitutive model.

The life model accounts for fatigue, creep, and environmental-fatigue damage under both isothermal and thermomechanical fatigue. At elevated temperatures, the damage terms must be calibrated to account for thermally activated damage mechanisms which change with increasing temperature. At lower temperatures and higher strain rates, fatigue damage dominates life prediction, while at higher temperatures and slower strain rates, environmental-fatigue and creep damage dominate life prediction. Under thermomechanical loading, both environmental-fatigue and creep damage depend strongly on the relative phasing of the thermal and mechanical strain rates, with environmental-fatigue damage dominating during out-of-phase thermomechanical loading and creep damage dominating in-phase thermomechanical loading.

The coarse-grained polycrystalline microstructure of the alloy studied causes a significant variation in the elastic response, which can be linked to the crystallographic orientation of the large grains. This variation in the elastic response presents difficulties for both the constitutive and life models, which depend upon the assumption of an isotropic material. The extreme effects of a large grained microstructure on the life predictions is demonstrated, and a suitable modeling framework is proposed to account for these effects in future work.

CHAPTER I

INTRODUCTION

1.1 Motivation

Gas turbine engines are used for power generation in many industries, including the energy and aerospace industries. Whatever the use for a gas turbine engine, increased efficiency is always a goal requiring more research. One method of increasing the efficiency of a gas turbine engine is to increase the operating temperature [1, 2]; however, the operating temperatures of gas turbine engines have reached and even surpassed the melting temperatures of the materials that come into direct contact with the hot gases in the engine [3]. These high operating temperatures can be achieved only by the use of advanced alloys that can withstand the harsh environment coupled with specially designed turbine blades that are internally cooled. When operating at these high temperatures, the turbine blades in the hot section of the engine undergo a complicated load history including cyclic temperature and stress.

For the safe and reliable design of the turbine components, it essential to be able to predict the material behavior and expected life under a wide range of thermomechanical fatigue (TMF) histories, in which temperature and load are changing simultaneously. The turbine blades also experience creep behavior caused by the high temperatures and sustained loads during operation.

In the past, fatigue life predictions have been made with empirical models based on expensive and time-consuming experiments. However, material behavior under variable load histories can be modeled with constitutive models, which in turn can be used to help predict life cycles to failure with a life model. These physically based models can be used to understand the physical mechanisms involved in fatigue, as

well as decrease the cost and time required to design new engine components.

1.2 Mar-M247 Material Specifications

The material of interest in this work is the Ni-based superalloy Mar-M247, which was developed by Danasi and Lund et al. at the Martin Metals Corporation in the 1970s [4, 5]. The Mar-M247 microstructure consists of a γ matrix strengthened by cubic γ' precipitates, the latter of which make up approximately 60 percent of the material by volume. With carbon present in the alloy, there are grain boundary carbides and script type MC carbides [6].

As shown in Figure 1.1, the grain size in the specimens used in this study were quite large, ranging nominally from 2 to 7 mm. This sizing is significantly greater than that reported on similar specimens for the same alloy studied by Boismier and Sehitoglu, which ranged from 0.2 to 2 mm [6]. The nominal chemical composition of Mar-M247 is given in Table 1.1.

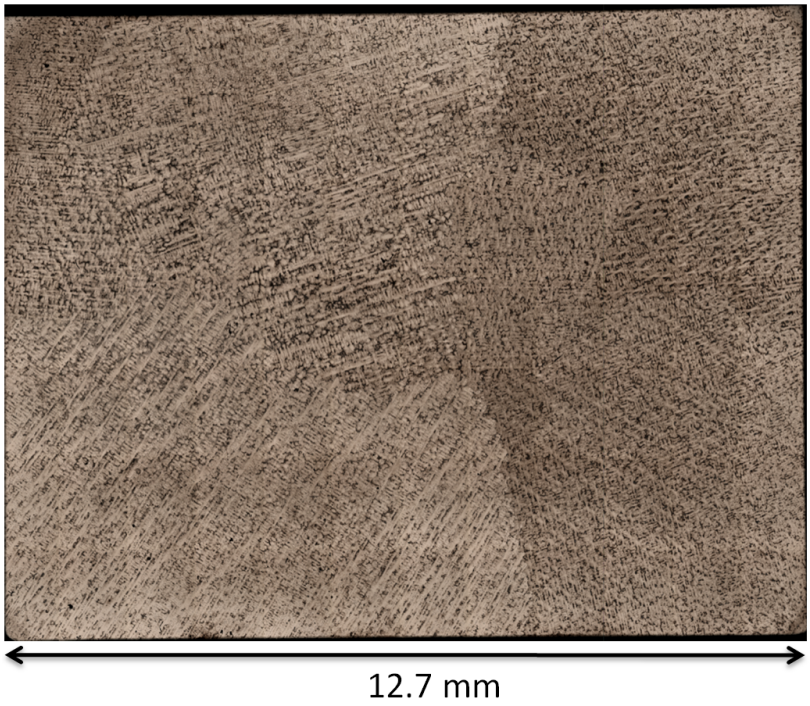

Figure 1.1: Example grain size – scale: 12.7 mm width. Optical microscopy image of microstructure exposed with Kalling's Etchant No. 1.

Table 1.1: Nominal chemical compositions of Mar-M247 & Mar-M002 given as percent by weight.

Alloy	C	Ni	Cr	Co	W	Al	Ta	Ti	Mo	Hf	B	Zr	Fe
Mar-M247	0.13	Bal.	8.4	10.0	10.0	5.5	3.0	1.0	0.65	1.4	0.015	0.05	<0.25
Mar-M002	0.15	Bal.	9.0	10.0	10.0	5.5	2.6	1.2	0.0	1.5	0.000	0.00	<1.0

Nickel-base superalloys are used in many high temperature applications requiring high strength, excellent creep resistance, and good resistance to hot corrosion [5]. The high temperature strength of Ni-base superalloys is attributable to the presence of the ordered $Ni_3(Al,Ti)$ γ' phase, which has an $L1_2$ structure.

In single crystalline superalloys, the material is highly anisotropic at low temperatures, typically below about 760°C. At higher temperatures, the deformation is mostly isotropic. The deformation mechanism at higher temperatures is largely governed by the by-pass of γ' particles by the dislocations, which homogenizes the macroscopic fatigue deformation response [7]. At temperatures above about 760°C, Ni-base superalloys are sensitive to strain-rate, but below this temperature they exhibit little strain-rate sensitivity [8].

In polycrystalline Ni-base superalloys, γ' particle size and carbides can have a large effect on strength. Increasing γ' particle size will lead to decreasing strength. Carbides provide additional strengthening by suppressing grain boundary sliding at elevated temperatures. Carbides can also play an important role in fracture as the initiation site of cracks [4].

1.3 Research Objective

The research presented in this thesis focuses on extending an existing unified constitutive and life model for the Ni-base superalloy Mar-M247 for use with a higher temperature. The existing constitutive model developed by Sehitoglu and Boismier is capable of predicting stress-strain response for isothermal fatigue (IF), in-phase

(IP) TMF, out-of-phase (OP) TMF, and TMF with more arbitrary temperature-load phasing for temperatures between 500° and 871° [9]. The existing life model is capable of predicting life to failure over the same temperature range for each of the listed types of fatigue tests using the stress-strain curve and load history provided by the constitutive model.

The goal of this work is to develop a constitutive and life model with similar capabilities over a wider temperature range of 500°C to 1038°C using the existing model as a starting point. Additionally, this research will apply the models to isothermal fatigue with dwells in order to incorporate the effects of creep. The specific research objectives are as follows:

1. Calibrate the unified constitutive model for a maximum temperature of 1038°C. The constitutive model should capture the stable stress-strain response of isothermal and thermomechanical fatigue as well as creep and stress-relaxation. The constitutive model must be sensitive to the effects of strain rate. Calibration will use isothermal tests at temperatures between 500°C and 1038°C at two different strain rates with and without dwells.

2. Validate the unified constitutive model under thermomechanical loading. Validation will use both IP and OP TMF tests.

3. Calibrate the life model. The life model should account for fatigue, creep, and environmental-fatigue damage under both isothermal and thermomechanical fatigue.

1.4 Thesis Layout

Chapter 2 is a background and literature review addressing thermomechanical fatigue, damage mechanisms found in Ni-base superalloys, and previous work in constitutive and life modeling. Chapter 3 presents the experimental methods used in this work,

including the specimens, experimental setup, and a summary of the experiments performed. Chapter 4 presents the constitutive model, the material parameters calibration, the variability found due to the coarse grained microstructure, the thermo-mechanical validation of the constitutive model, and finally the implementation of the constitutive model in a fully 3-dimensional form. Chapter 5 presents the life model, starting with the damage terms and ending with a description of how the damage terms interact and life predictions for the load histories considered. Finally, Chapters 6 and 7 conclude this work with the conclusions and recommendations for further work, respectively.

CHAPTER II

BACKGROUND

2.1 Thermomechanical Fatigue

Thermomechanical fatigue is fatigue under simultaneous temperature and mechanical strain cycles [10]. In gas turbine engines, thermomechanical loading conditions are caused by the variation in applied load and thermal gradients in the engine components during operation. In gas turbines, the times of greatest change in load and temperature typically occur during engine startup and shutdown [10]. During engine operation, the load seen by components can also be related to creep or stress-relaxation at elevated temperatures.

Although data for isothermal fatigue is often widely available at a variety of temperatures, the damage seen under TMF cannot generally be directly related to IF data [11, 12]. Indeed, many authors have shown that the use of IF data taken at the maximum temperature of a TMF cycle can result in non-conservative life predictions [13–21]. Because of this, it is necessary to perform separate TMF tests in order to accurately predict life under TMF loading conditions. There are many possible temperature and load combinations possible for TMF tests; however, there are two that are the most common: in-phase and out-of-phase loading [22]. An example of these load histories is shown in Figure 2.1.

Under IP loading, the peak temperature and mechanical load are in sync. Under OP loading, the peak temperature and mechanical load are 180° out of sync. A mechanical load can refer to an applied force or mechanical strain. Another common TMF load history is the diamond waveform, where the peak temperature and mechanical load are between 0° and 180° out of sync. The phase angle between the

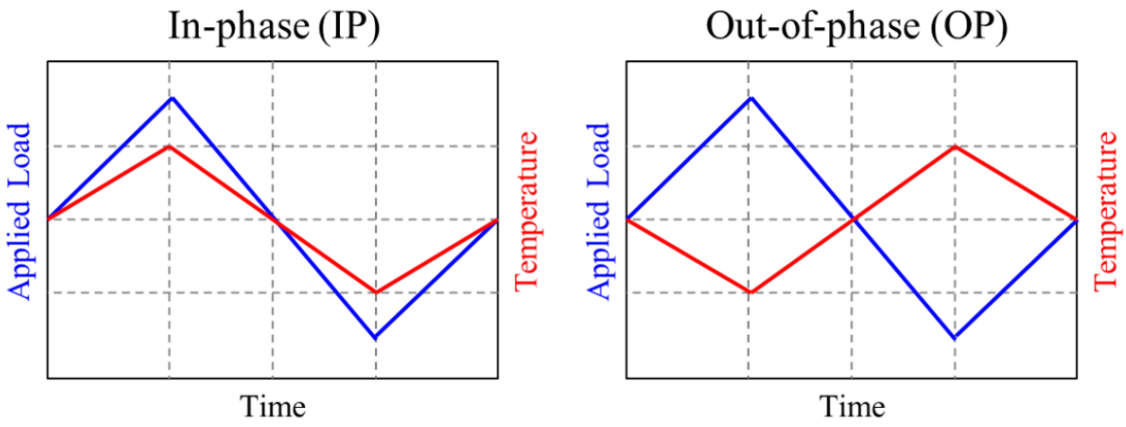

Figure 2.1: Out-of-phase (OP) and in-phase (IP) TMF cycles with linear waveforms [22].

temperature and mechanical load waveforms is important because it determines the type of damage mechanisms that are active in the material.

2.2 Damage Mechanisms

There are three important damage mechanisms that affect the life of Ni-base superalloys under high temperature thermomechanical fatigue: fatigue, environment-fatigue interaction, and creep [9, 23–25]. These three damage mechanisms may interact depending on the temperature, mechanical load, and the phase angle between temperature and mechanical load waveforms. Due to the time and temperature dependent nature of the environment-fatigue interactions and creep damage, thermomechanical fatigue in Ni-base superalloys is highly dependent on the path history of thermal and mechanical load [26]. Common interactions are pure fatigue, fatigue and environmental-fatigue interactions, and fatigue and creep [9, 12, 24].

In ductile solids, fatigue damage is caused by the accumulation of irreversible shear displacements along crystallographic slip planes during cyclic loading. Fatigue damage alone, without interactions from other types of damage, is found at relatively low temperatures and at high applied strain rates where the inelastic deformation is typically time-independent. At lower temperatures and high strain rates, damage

from time dependent mechanisms such as creep and environmental effects are typically negligible. [7, 12].

Environmental-fatigue damage can occur when the material is exposed to a reactive ambient atmosphere at elevated temperatures [9, 24]. At elevated temperatures, the material constituents have sufficient thermal energy to undergo oxidation with environmental species. In the case of Ni-base superalloys, several different oxides can form at or near the surface of the material. These oxides are quite brittle in comparison to the substrate material [27]. Since the superalloys often have ten or more elemental constituents and multiple phases, the chances of promoting a sustainable reaction are high and can result in complex oxide formation. [1, 24, 27]. Since the damage is caused by oxidation and the interaction of the oxides with cyclic loading, this damage mechanism is highly time-dependent.

Creep damage is caused by time-dependent diffusional processes which are activated at higher temperatures [28]. Many mechanisms have been proposed to explain creep damage. Different mechanisms of creep damage are expected to operate under IF and TMF conditions, and oxidation may aid in the creep processes. [9]. For Mar-M247 creep damage has been observed in the form of internal intergranular cracking and void formation [9, 11, 12, 29]. The growth and coalescence of these cracks occur predominantly under tensile loading [11, 12, 20, 30–34].

2.2.1 Pure Fatigue Damage

Pure fatigue damage typically only occurs at low temperatures and high strain rates when environmental interactions and creep mechanisms are inactive. Damage occurs under cyclic straining with the accumulation of irreversible dislocation motion. This results in dislocation slip along glide planes and corresponds to shear displacements. With sufficiently high plastic strain, a nominal measure of damage accumulation is the cumulative plastic strain since a significant fraction of dislocation motion will be

irreversible at high strains. This nominal measure is only an approximate measure of the global fatigue damage. [7]

In single crystals, the dislocation motion results in localized slip bands. These slip bands form visible markings on the surface of the material. If a specimen is polished to remove the slip band markings and then cycling is continued, the marking will return in the same location as before. Because of this observed behavior, the markings were given the name "persistent slip bands" (PSB). It has been demonstrated that this behavior is due to the fact that PSB's are formed in the bulk of a single crystal and are visible as markings along the surface [7]. At high enough reversed plastic strains, PSB's will eventually form extrusions and intrusions which act as stress concentrations and serve as crack initiation locations [2, 7, 23, 24].

For polycrystalline materials, the presence of precipitates, impurities, inclusions, and grain boundaries may cause fatigue mechanisms to differ from that of single crystals. The fatigue mechanisms at the surface of a polycrystalline material, however, may be related to those observed in single crystals. For example, PSB's can still form in the bulk of polycrystalline metals, but surface markings will not appear unless a PSB forms in a grain at the surface of the material. [7]

Many empirical approaches have been used to estimate fatigue life. In the high-cycle regime where there is little plastic deformation, the simplest life model is Basquin's rule, which relates the stress amplitude to life with a power law relationship

$$\sigma_a = \sigma'_f \left(2N_f\right)^b \tag{2.1}$$

where σ'_f and b are material constants, σ_a is the stress amplitude, and $2N_f$ is the fatigue life measured in the number of reversals to failure. In the low-cycle regime, the corresponding power law relationship that relates the plastic strain amplitude to life is known as the Coffin-Manson expression

$$\epsilon_{pl,a} = \epsilon'_f \left(2N_f\right)^c \tag{2.2}$$

where ϵ'_f and c are material constants and $\epsilon_{pl,a}$ is the plastic strain amplitude. The high-cycle and low-cycle regimes may be combined using Hooke's law to form one equation

$$\Delta\epsilon_a = \frac{\sigma'_f}{E}\left(2N_f\right)^b + \epsilon'_f\left(2N_f\right)^c \tag{2.3}$$

where E is the elastic modulus. Since the above life models do not include the effects of mean stress, many models have been proposed to include mean stress into the life models. The Soderberg and Goodman models are two such examples which relate the relative damage caused by mean stress and alternating stress. These models can then be included in the life model to form a life model which includes the effects of mean stress. The Smith-Watson-Topper life model is a popular model which indirectly accounts for mean stress through the maximum stress as

$$\sigma_{max}\epsilon_a = \frac{\left(\sigma'_f\right)^2}{E}\left(2N_f\right)^{2b} + \sigma'_f\epsilon'_f\left(2N_f\right)^{b+c} \tag{2.4}$$

where σ_{max} is the maximum stress and ϵ_a is the mechanical strain amplitude. [35]

2.2.2 Environmental-Fatigue Damage

Environmental-fatigue damage occurs when a material oxidizes and the oxide layers interact with mechanical and thermal loading. There are several different mechanisms which can cause damage, including oxide spiking and oxide spallation.

Oxide spiking occurs when oxide layers crack and expose the unoxidized material underneath, which then oxidizes and cracks. Eventually, through repeated oxidation and cracking, oxide spikes are formed which can extend into the bulk of the material as seen in Figure 2.2a [25]. The oxide layer may crack for multiple reasons. Typically, the oxide layers are more brittle than the matrix and bulk material, and consequently have a lower fracture toughness. Additionally, the oxide layers have different elastic and thermal properties, which cause strain mismatches between the oxide layer and the matrix. This causes additional stress in the oxide layer and can lead to brittle fracture [36–38]. Oxide spikes extending into the bulk material can lead to macro scale

cracks which can grow to the critical crack length causing failure. Figure 2.3 shows an example of oxide spike formation in a directionally solidified Ni-base superalloy [39].

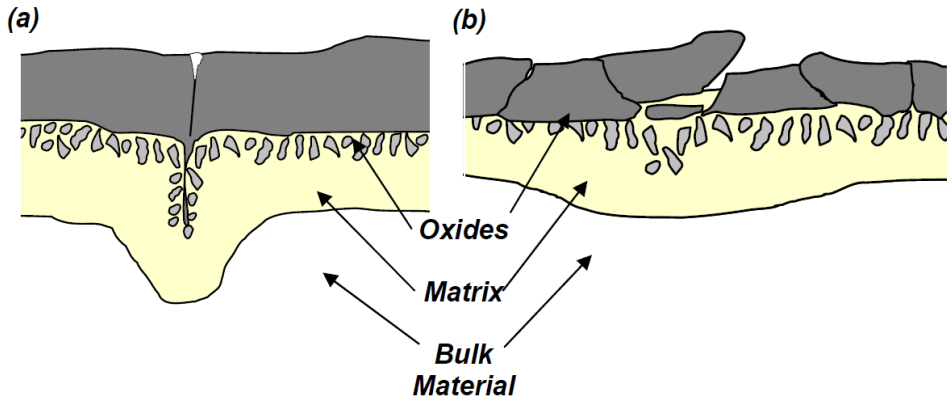

Figure 2.2: Surface oxidation and mechanical interaction in intermetallic superalloys (a) oxide spiking and (b) oxide spallation [25].

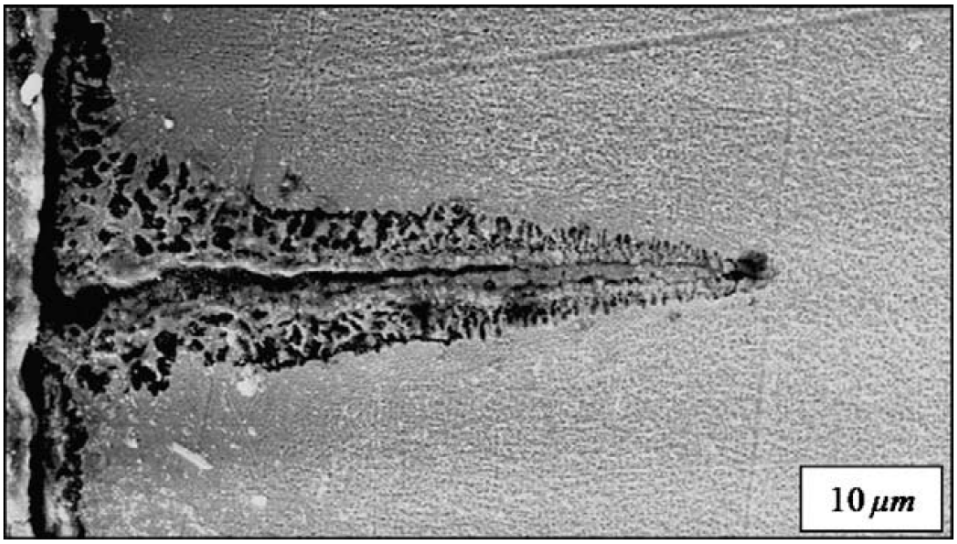

Figure 2.3: Smooth specimen crack initiation at an oxide spike in longitudinal CM247LC DS under OP TMF [39].

Oxide spallation is the result of oxide layers forming wedges during compressive loading and thermal strain mismatches [38, 40, 41]. The oxide wedges can be seen in Figure 2.2b. Once formed, oxide wedges can detach or spall at the interface between the oxide and matrix and expose the unoxidized material. Adherent oxides may form

on bare Ni-base superalloys [42–45], as well as coated Ni-base superalloys [46]. Adherent oxide scales can cause surface roughening and pitting which leads to increased oxidation rates and promotes crack initiation [25].

2.2.3 Creep Damage

The time dependent creep damage in Mar-M247 is related to the formation of internal intergranular cracking and void formation during tensile loading. Embrittlement of grain boundaries due to oxidation will also aid the creep process [9]. Since creep damage depends on diffusional processes, it requires higher temperatures to activate. In Mar-M247, creep damage can be found in specimens subjected to temperatures over 500°C [6]. Figure 2.4 shows creep damage in the form of internal intergranular cracking found by Boismier and Sehitoglu for Mar-M247 [9].

Figure 2.4: Intergranular crack growth in Mar-M247 under IP TMF loading ($T_{min} = 500°C, T_{max} = 871°C$) [9].

Kupkovits and Neu performed thermomechanical fatigue tests on smooth and notched specimens of directionally solidified Ni-base superalloy CM247LC DS [39]. In both the smooth and notched specimens, they found internal voids caused by creep damage under IP TMF loading. Figure 2.5 shows the internal voids in both smooth and notched specimens [39].

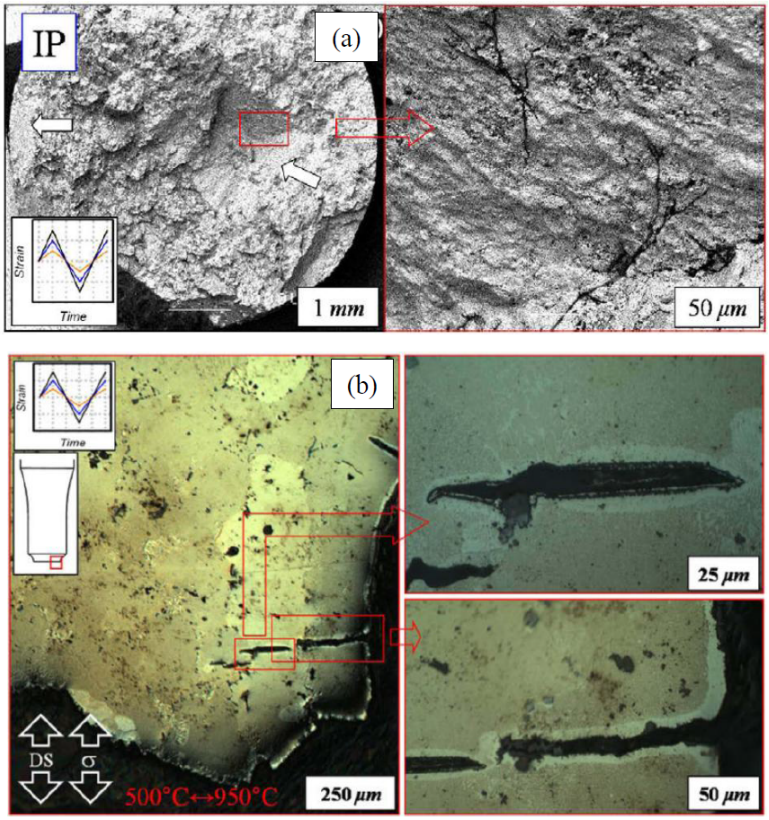

Figure 2.5: Internal voids from creep damage: (a) smooth specimen with crack initiation sites indicated by a white arrow and (b) notched specimen [39].

Additional potential creep damage mechanisms are magnified crack tip plasticity resulting from the plastic zones of voids ahead of a crack, grain boundary sliding initiating wedge-type cracks at grain boundaries and at hard second-phase particles on the grain boundaries, grain boundaries acting as weak paths for flow localization and crack growth, and the modification of the crack tip strain fields in the absence of cavities [9].

2.3 Previous Work

This work is based on the previous constitutive and life modeling performed by Slavik and Sehitoglu [47, 48], Neu and Sehitoglu [12, 49], and Boismier and Sehitoglu [6, 9]. The original models were formulated for 1070 steel and then used and calibrated for Mar-M247. The ultimate goal of estimating component life consists of two parts: a

constitutive model used to predict the stress-strain history and a life model used to predict cycles to failure based on the stress-strain-temperature history.

2.3.1 Constitutive Models

Slavik and Sehitoglu sought to establish a constitutive model capable of accurately predicting eight different behaviors [47]:

1. Cyclic transient hardening or softening to a stable state where the transient rate is dependent on strain and temperature.
2. Mean stress relaxation under mean strain cycling.
3. Strain rate sensitivity.
4. Strain ratcheting under mean stress cycling.
5. Stress relaxation under strain holds.
6. Creep behavior under stress holds at high temperatures.
7. Metallurgical changes due to aging, thermal recovery, and phase transformations.
8. Material behavior under complex temperature and strain histories.

Although many constitutive models exist that treat some of the material response characteristics listed above [50–68], these models cannot simulate stress relaxation under strain holds, creep straining for stress holds, strain rate sensitivity, or time dependent metallurgical changes. The model established by Slavik and Sehitoglu accounts for mean stress relaxation under mean strain cycling, strain rate sensitivity at different temperatures, stress relaxation under strain holds, effects caused by strain aging, and material behavior under complex temperature and strain histories [48]. Figure 2.6 shows the ability of the Slavik-Sehitoglu model in capturing mean stress

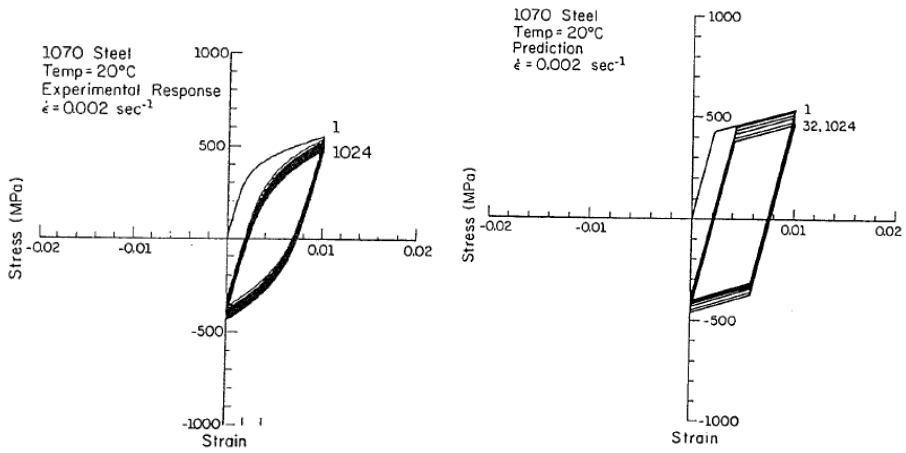

(a) Experiment **(b)** Model

Figure 2.6: Mean stress relaxation modeled by Slavik and Sehitoglu for 1070 steel [48].

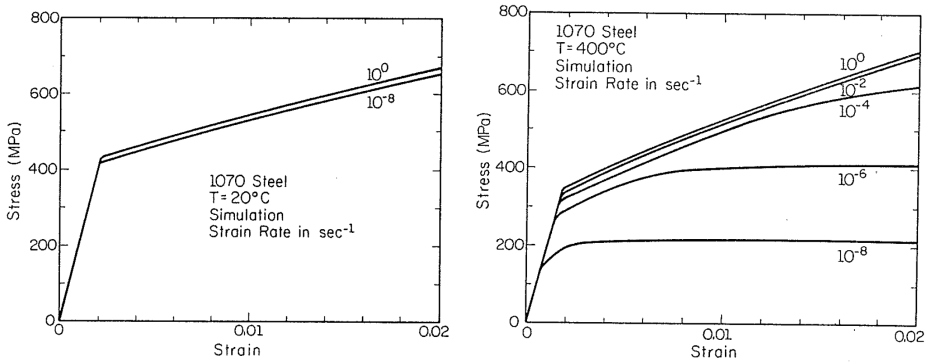

(a) Rate dependence at 20°C **(b)** Rate dependence at 400°C

Figure 2.7: Rate and temperature dependence modeled by Slavik and Sehitoglu for 1070 steel [48].

relaxation [48]. Figure 2.7 shows the ability of the Slavik-Sehitoglu model to capture rate sensitivity at two different temperatures [48].

The Sehitoglu-Boismier unified constitutive model [9] is based on the work of Slavik and Sehitoglu [47, 48], which established the constitutive model for 1070 steel using internal state variable theory and experiments designed to isolate the various evolving parameters, as well as establish the form of the flow rule. Boismier and Sehitoglu were able to apply this constitutive model to Mar-M247 and successfully predict the same types of material behavior [6, 9]. Figure 2.8 shows the ability of

the constitutive model used by Boismier and Sehitoglu to simulate thermomechanical load histories.

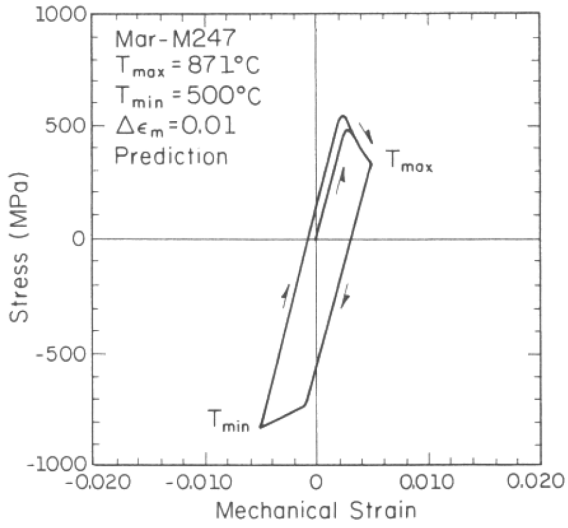

Figure 2.8: Prediction of in-phase TMF response by Boismier and Sehitoglu for Mar-M247 [9].

2.3.2 Life Models

Neu and Sehitoglu developed a life model for 1070 steel which incorporated damage caused by fatigue, environmental attack, and creep [12, 49]. This work was driven by a need to develop a life model capable of handling different damage mechanisms that may change with changing load conditions, especially at high temperatures and with variable temperature-strain histories. Previous life models consider a variety of damage mechanisms, but are not applicable outside the range of load histories from the experiments used to derive the life model. Many of the early environmental life models include damage mechanisms associated with oxidation, but neglect creep [69–72], while many creep-fatigue models do not treat oxidation damage separately [32, 73, 74].

The Neu-Sehitoglu life model identifies the various physical damage mechanisms and then relates them to a measure of life, combining them in a way that may be used for life prediction without prior knowledge of which damage mechanisms may

be active for the load history of interest. The damage terms are related linearly, and summed to obtain the total damage on a per cycle basis, D^{tot}:

$$D^{tot} = D^{fat} + D^{ox} + D^{creep} \tag{2.5}$$

where the superscripts "fat", "ox", and "creep" represent fatigue, oxidation, and creep, respectively [12]. Assuming that damage is equal to 1 at failure and that the damage is related linearly as above, the damage equation can be re-written in terms of life:

$$\frac{1}{N_f} = \frac{1}{N_f^{fat}} + \frac{1}{N_f^{ox}} + \frac{1}{N_f^{creep}} \tag{2.6}$$

where N_f is the failure life [12].

Boismier and Sehitoglu applied this life model to Mar-M247 to predict life for isothermal fatigue, in-phase thermomechanical fatigue, out-of-phase thermomechanical fatigue, and thermomechanical fatigue with a diamond shaped load-temperature history [9]. Figure 2.9 shows the life prediction of the Boismier-Sehitoglu life model for an out-of-phase thermomechanical load history.

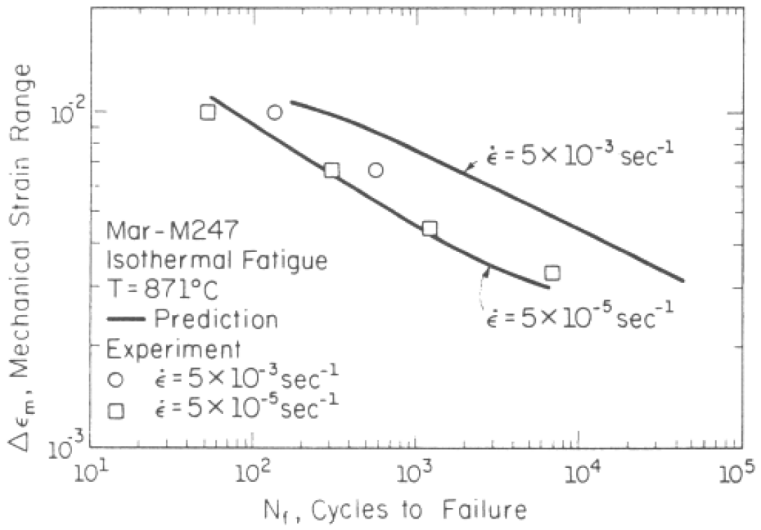

Figure 2.9: Prediction of OP TMF by Boismier and Sehitoglu for Mar-M247 [9].

The physical mechanisms for each damage term were discussed in Section 2.2, where the oxidation damage term of the Neu-Sehitoglu life model corresponds to

the environmental-fatigue interaction damage mechanisms. The particular equations used to characterize the three damage terms of this work will be discussed further in Chapter 5.

CHAPTER III

EXPERIMENTAL METHODS

In order to explore the three damage mechanisms mentioned in Chapter 2, three types of fatigue tests were performed. Isothermal fatigue tests, isothermal fatigue tests with dwells, and thermomechanical fatigue tests were performed at two strain rates over a variety of temperatures ranging from 500°C to 1038°C.

3.1 Specimens

The specimens were machined from vacuum melted and cast bars following the ASTM E606-12 guidelines. The resulting smooth cylindrical dogbone test specimens had a gage section of 12.7 mm and a 6.35 mm gage diameter. The specimens were given a standard proprietary heat treatment for turbine blade and vane components. The received specimens contained equiaxed, extremely large grains, from 2 to 7 mm in diameter. Due to the size of the grains, it is likely that the gage section of the specimens contained fewer grains than the ASTM E606-12 required minimum of ten grains for nominally homogeneous materials. As a result, these large grains had a significant effect on the observed elastic modulus of the test specimens which will be discussed in Chapter 4.

3.2 Experimental Setup

TMF experiments were conducted on a 44-kN MTS servo-hydraulic test system with a Flextest 40 controller and Multipurpose Elite controller software. Strain during the experiments was measured with a 632.52E-14 MTS high temperature extensometer. The specimens were heated using an Ameritherm 2 kW induction heater, and the temperature controlled via K-type thermocouples in conjunction with a Watlow 945A

PID temperature controller. Hysteresis in the thermal strain was compensated for through a time based compensation scheme discussed elsewhere [24].

3.3 Experiments

In total, 18 tests were performed as a part of this work: ten IF tests, four IF tests with dwell periods (referred to as dwell tests in this thesis to distinguish them from the IF tests), and four TMF tests. Each of the 18 tests was performed under mechanical strain control. Fatigue life was defined as the number of cycles required to initiate a fatigue crack. The criterion used to determine the number of cycles to crack initiation was defined as the number of cycles to reach a 50% load drop from the extended maximum load limit. The IF tests were performed at two different strain rates and at five different temperatures to capture the temperature and time-dependent behavior. The IF test matrix is given in Table 3.1.

Table 3.1: Isothermal fatigue calibration experiments.

Temperature [°C]	$\mathbf{\Delta\epsilon_{mech}}$ [%]	$\mathbf{R_\epsilon}$	**Strain Rate** $\left[\frac{\mathbf{1}}{\mathbf{s}}\right]$
500	1.4	-1	5.00×10^{-3}
871	1.2	-1	5.00×10^{-3}
927	0.8	-1	5.00×10^{-3}
982	0.8	-1	5.00×10^{-3}
1038	0.6	-1	5.00×10^{-3}
500	1.4	-1	5.00×10^{-5}
871	1.0	-1	5.00×10^{-5}
927	0.8	-1	5.00×10^{-5}
982	0.8	-1	5.00×10^{-5}
1038	0.7	-1	5.00×10^{-5}

The dwell tests were performed at the four higher temperatures from the IF tests. An intermediate strain rate was used for the dwell tests with a dwell time of 600

seconds at the maximum strain of the cycle. The dwell test matrix is given in Table 3.2.

Table 3.2: Dwell calibration experiments.

Temperature [°C]	$\mathbf{\Delta\epsilon_{mech}}$ [%]	$\mathbf{R_\epsilon}$	**Strain Rate** $\left[\frac{\mathbf{1}}{\mathbf{s}}\right]$	**Dwell Time** [s]
871	1.0	-1	5.00×10^{-4}	600
927	0.8	-1	5.00×10^{-4}	600
982	1.0	-1	5.00×10^{-4}	600
1038	0.8	-1	5.00×10^{-4}	600

After calibrating the constitutive model, the TMF verification tests were performed. The TMF tests were performed over the full temperature range of 500 to 1038°C. Two tests were performed with an in-phase (IP) temperature history, and two with an out-of-phase (OP) temperature history at a mechanical strain rate of $3.33 \times 10^{-5} s^{-1}$. The TMF verification test matrix is given in Table 3.3.

Table 3.3: TMF verification experiments.

Specimen ID	**Temperature Range** [°C]	**Phase**	$\mathbf{\Delta\epsilon_{mech}}$ [%]	$\mathbf{R_\epsilon}$	**Strain Rate** $\left[\frac{\mathbf{1}}{\mathbf{s}}\right]$
JF21	500–1038	IP	1.05	-1.1	3.33×10^{-5}
JF20	500–1038	OP	1.0	-1.0	3.33×10^{-5}
JF30	500–1038	IP	0.5	0.0	3.33×10^{-5}
JF29	500–1038	OP	0.5	-1.0	3.33×10^{-5}

CHAPTER IV

CONSTITUTIVE MODEL

4.1 Unified Thermo-Viscoplasticity Constitutive Model

The constitutive equation used in this work is based on the Slavik-Sehitoglu unified viscoplasticity constitutive model originally developed for 1070 steel [12]. The total strain rate is decomposed into elastic, inelastic, and thermal strain rate components,

$$\dot{\epsilon}_{ij} = \dot{\epsilon}^{e}_{ij} + \dot{\epsilon}^{in}_{ij} + \dot{\epsilon}^{th}_{ij} \tag{4.1}$$

The thermal strain rate is given by,

$$\dot{\epsilon}^{th}_{ij} = q_{CTE}\dot{T}\delta_{ij} \tag{4.2}$$

where q_{CTE} is the coefficient of thermal expansion that may be temperature dependent, and δ_{ij} is Kronecker's delta. The elastic strain rate is given by

$$\dot{\epsilon}^{e}_{ij} = \frac{1}{E}\left[(1-\nu)\,\dot{\sigma}_{ij} - \nu\dot{\sigma}_{kk}\delta_{ij}\right] - \left[(1-\nu)\,\sigma_{ij} - \nu\sigma_{kk}\delta_{ij}\right]\frac{\partial E}{\partial T}\frac{\dot{T}}{E^2} \tag{4.3}$$

where it is assumed that Poisson's ratio, ν, is independent of temperature. The inelastic flow rule is given as

$$\dot{\epsilon}^{in}_{ij} = \frac{3}{2}f\left(\frac{\bar{\sigma}}{K}\right)\frac{S_{ij}-\alpha_{ij}}{\bar{\sigma}} \tag{4.4}$$

where the flow function, f, is given by

$$f\left(\frac{\bar{\sigma}}{K}\right) = \begin{cases} A\left(\frac{\bar{\sigma}}{K}\right)^{n_1} & for \frac{\bar{\sigma}}{K} \leq 1 \\ Aexp\left(\left(\frac{\bar{\sigma}}{K}\right)^{n_2} - 1\right) & for \frac{\bar{\sigma}}{K} > 1 \end{cases} \tag{4.5}$$

The leading coefficient, A, of the flow function is a function of temperature, with temperature given in kelvins.

$$A = A'_c exp\left(-\frac{\Delta H}{RT}\right) \tag{4.6}$$

In Equations 4.4 and 4.5, K denotes the drag stress state variable, S_{ij} denotes the current deviatoric stress, α_{ij} denotes the current deviatoric back stress state variable, and the effective stress, $\bar{\sigma}$, is

$$\bar{\sigma} = \left[\frac{3}{2}\left(S_{ij} - \alpha_{ij}\right)\left(S_{ij} - \alpha_{ij}\right)\right]^{\frac{1}{2}} \tag{4.7}$$

The two state variables, drag stress and back stress, represent isotropic and kinematic hardening respectively. Since the aim of the thermo-viscoplasticity model is to capture the stabilized cyclic response, the drag stress is taken to be the saturated drag stress that varies with temperature only [9]. Back stress evolves according to

$$\dot{\alpha}_{ij} = \frac{2}{3} h_\alpha \dot{\epsilon}^{in}_{ij} - r_\alpha \alpha_{ij} \tag{4.8}$$

The back stress hardening coefficient, h_α, and the back stress thermal recovery coefficient, r_α, are given by

$$h_\alpha = \begin{cases} \left(a_\alpha - b_\alpha |\bar{\alpha}|\right) & \alpha_{ij}\dot{\epsilon}^{in}_{ij} \geq 0 \\ a_\alpha & \alpha_{ij}\dot{\epsilon}^{in}_{ij} < 0 \end{cases} \tag{4.9}$$

$$r_\alpha = c_\alpha \left(\bar{\alpha}\right)^{d_\alpha} \tag{4.10}$$

where all of the parameters, a_α, b_α, c_α, and d_α may be temperature dependent. For back stress thermal recovery, d_α is a constant and the parameter c_α accounts for temperature dependent behavior according to an Arrhenius type equation. In Equations 4.9 and 4.10, $\bar{\alpha}$ is the effective back stress defined as

$$\bar{\alpha} = \left(\frac{3}{2}\alpha_{ij}\alpha_{ij}\right)^{\frac{1}{2}} \tag{4.11}$$

The parameters n_1, n_2, A'_c, and ΔH in the preceding equations are material constants that were calibrated to Mar-M247 over the temperature range of 500°C to 871°C by Boismier and Sehitoglu [9], and are re-calibrated to the temperature range of 500°C to 1038°C in this work. The constant R is the molar gas constant and the parameters a_α and b_α are functions of temperature determined in this work.

It was found that the Slavik-Sehitoglu back stress hardening equation [48] did not accurately model the behavior of Mar-M247 at the higher temperatures. By allowing the parameters a_α and b_α to vary with temperature independently, the form of the back stress hardening equation could be used to capture the behavior of Mar-M247 at higher temperatures.

A third form for back stress hardening was also briefly considered from the work of Slavik and Cook [75]. Slavik and Cook used this form to calibrate the constitutive model for René 80. This form of the back stress hardening equation proved difficult to calibrate for Mar-M247 because a reasonable calibration required the parameters to depend on strain rate as well as temperature.

This constitutive equation was first calibrated from the IF and dwell experiments using a one-dimensional Matlab function for uniaxial loading. Once the equation had been fully calibrated for uniaxial TMF loading, a fully three-dimensional ABAQUS User MATerial subroutine (UMAT), coded in FORTRAN, generalized the thermo-viscoplasticity constitutive model for three-dimensional TMF loadings.

4.2 Material Parameters Calibration

The viscoplastic parameters were calibrated through an iterative process. First, the model sensitivity to a_α, b_α, and n_1 was explored. In the calibration process, the measured elastic modulus of each specimen was used due to the wide variability seen among the specimens. Then the parameters a_α and b_α were calibrated discretely at each temperature for the best match to the experimental isothermal fatigue data using the original value for n_1. This was accomplished by iteratively plotting all of the responses at a given strain rate and comparing them against the experimental data until a satisfactory match was made considering the important features of the plot, such as elastic-plastic transition and maximum and minimum stress. Having adjusted the parameters a_α and b_α for one strain rate, the predicted response could be compared

to the experimental data at the second strain rate to adjust n_1 appropriately. Upon updating the flow rule exponent, the parameters determining A were adjusted to minimize the error from the flow rule plot in Figure 4.1.

When the three parameters allowed satisfactory prediction of the experimental isothermal fatigue data, the dwell response was predicted and compared to the experimental dwell data. This comparison allowed final adjustments to be made to n_1 such that the response of the strain hold could be satisfactorily predicted. In this final step, it was found that the back stress thermal recovery coefficient was unnecessary since the model already satisfactorily predicted the stress relaxation, therefore c_α was set to zero. Finally, the temperature dependent values for the parameters a_α and b_α were curve fit to find the temperature-dependent functions.

A plot of Equation 4.4 is shown in Figure 4.1 along with experimental data points used to determine this fit. In this plot the strain rate normalized with the flow rule coefficient is plotted against the effective stress normalized with the drag stress. The slope of the flow rule for values of effective stress divided by drag stress less than unity is determined by n_1, while the slope of the flow rule for values greater than unity is determined by n_2. The experimental data plotted uses the effective stress from the 0.02% yield point on the second cycle of the fully-reversed uniaxial fatigue tests and the strain rate of the test.

Extending the thermo-viscoplasticity model to elevated temperatures necessitated several changes in the functional forms and parameters from the original model calibrated by Boismier and Sehitoglu [9]. One of the more significant changes was the reduction in the exponent in the power law (creep) factor of the flow rule to capture the increased rate sensitivity at higher temperatures.

Figure 4.2 shows the flow rule for Mar-M247 used by Boismier and Sehitoglu [9]. The most obvious difference between the flow rule of Boismier and Sehitoglu and the flow rule used in this thesis is the slope of the flow function for values of $\frac{\bar{\sigma}}{K}$ less than

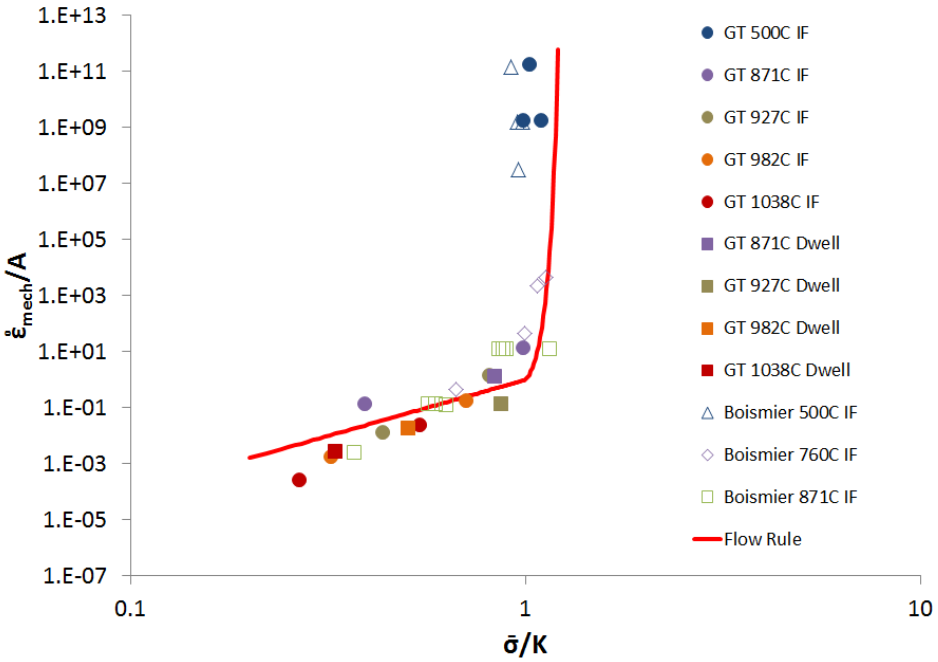

Figure 4.1: Experimentally determined flow rule function.

unity. Where Boismier and Sehitoglu used a value for n_1 of 11.6 [9], this work reduced the value of n_1 to 4.0. The need for this change was driven by the larger temperature range under consideration. Between the two flow rules, the value for n_2 remained the same, but the calibration of the coefficient A had to be updated to be consistent with the change in n_1.

While the experimental data shown in Figure 4.1 was used to help calibrate the flow rule, many combinations of n_1, A_c', and ΔH from Equations 4.5 and 4.6 can be used to make reasonable fits through the experimental data. Reasonable fits can be obtained for values of n_1 ranging from 4.0 to 9.6, with the proper adjustment to A_c' and ΔH. The flow rule calibration plot of Figure 4.1 is not the complete calibration for the stress-strain prediction, however. The hardening laws must also be considered for the complete calibration. When calibrating the whole model to the stress-strain curves, it was found that a lower value for n_1 allowed for a better overall calibration to the stress-strain experimental curves. Using this value for n_1, it was found that no

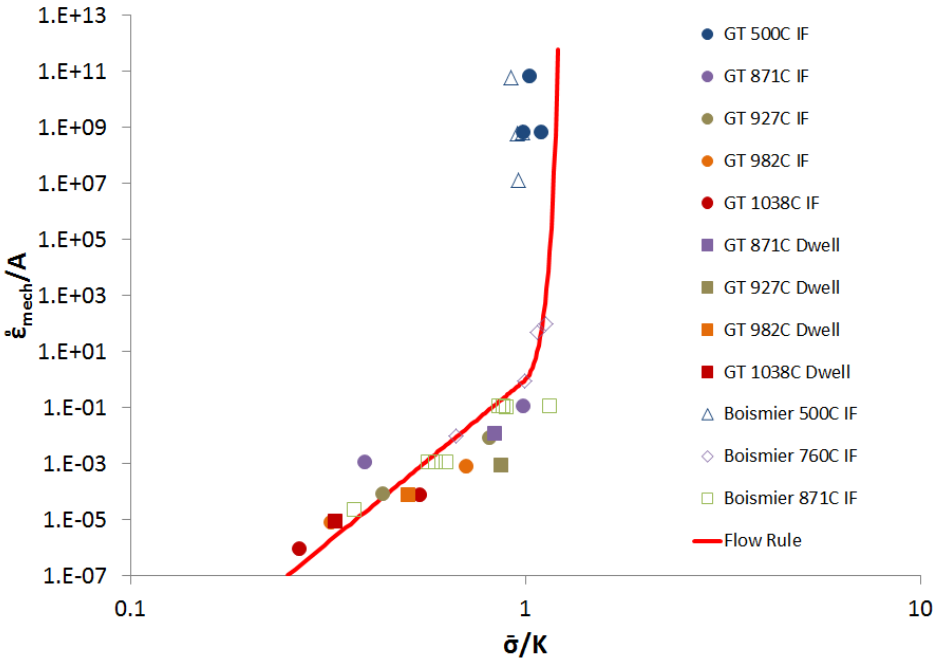

Figure 4.2: Flow rule function used by Boismier and Sehitoglu [9].

back stress thermal recovery term was necessary to capture the stress relaxation in a strain hold.

The calibrated values for the flow rule constants of Equation 4.4 are listed in Table 4.1. The temperature dependent parameters for the flow rule and back stress, as well as the saturated drag stress equations are given in Table 4.2. The back stress hardening coefficients a_α and b_α are highly dependent on temperature, as shown in Figure 4.3. The elastic properties and coefficient of thermal expansion are given in Table 4.3.

Table 4.1: Flow rule parameters.

$\mathbf{n_1}$	$\mathbf{n_2}$	$\mathbf{A_c'}$	$\frac{\mathbf{\Delta H}}{\mathbf{R}}$
$[-]$	$[-]$	$[s^{-1}]$	$[K]$
4.0	17.5	4.549×10^{17}	55499

Table 4.2: Hardening parameters. Temperatures in °C.

Parameter	Equation	Units
Sat. Drag Stress:	$K_{sat} = 886.1 - 0.376T$	[MPa]
	$a_\alpha = 30774 + 464T - 3.916 \times 10^{-1}T^2$	[MPa]
Back Stress Hardening Coefficients:	$b_\alpha = \begin{cases} 10054 - 22.8T + 1.34 \times 10^{-2}T^2 & 500 \leq T < 927°C \\ -5895.5 + 6.818T & 927 \leq T < 982°C \\ 800 & 982 \leq T \leq 1038°C \end{cases}$	[–]

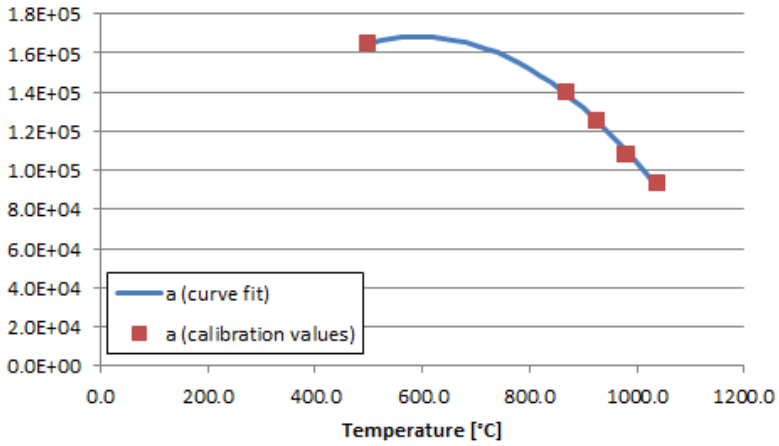

(a) Back stress hardening coefficient a_α.

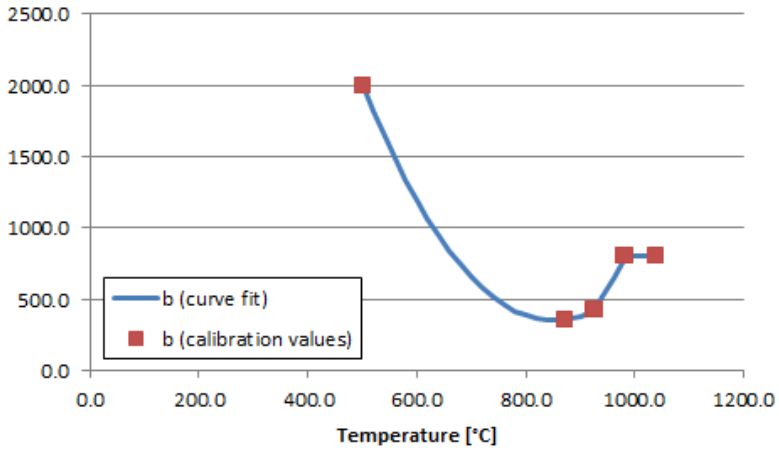

(b) Back stress hardening coefficient b_α.

Figure 4.3: Temperature dependence of backstress hardening coefficients.

Table 4.3: Elastic and thermal expansion properties. Temperatures in °C.

Parameter	Equation	Units
Elastic Modulus	$E = 253900 - 107.8T$	[MPa]
Elastic Shear Modulus	$\nu = 0.3$	[–]
Coefficient of Thermal Expansion	$q_{CTE} = 1.885 \times 10^{-5}$	$\left[\frac{1}{^\circ C}\right]$

4.3 Calibration Plots

The half-life responses from the isothermal fatigue calibration experiments are plotted with the calibrated model predictions in Figure 4.4. Because of the variability in the elastic modulus from specimen to specimen, the actual measured elastic modulus is used to correctly determine the inelastic response in the calibration phase. The model captures the strain rate sensitivity and temperature sensitivity, as well as the influence of the dwell, with emphasis placed on predicting the relaxed stress value at the end of the dwell as shown in Figure 4.5.

No dwell test was run for a temperature of 500°C, but the model was run at this temperature to show that the model appropriately captures temperature sensitivity. Figure 4.6 shows the model's prediction for a dwell test at 500°C. As one would expect for the relatively low temperature of 500°C, the model predicts very little stress relaxation.

It may be possible to better capture the material behavior shown in the experimental data from this work; however, the form of the constitutive equation must be updated or changed to achieve this goal. Since the scope of this work was only to extend an existing model to a greater temperature range, no attempt was made to determine a more appropriate form of the constitutive equation that could capture the material behavior shown over the larger temperature range of 500°C to 1038°C. It is anticipated, however, that such an equation would require an additional temperature dependent term to account for changing deformation mechanisms.

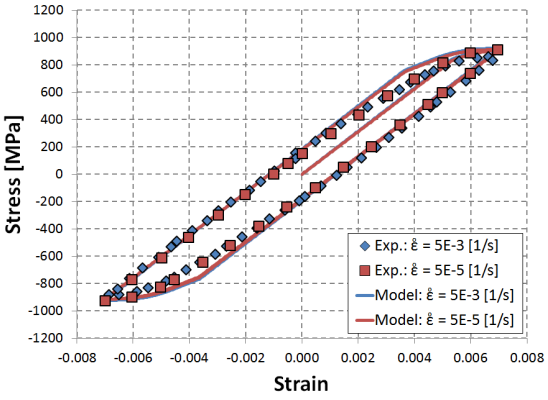

(a) 500°C.

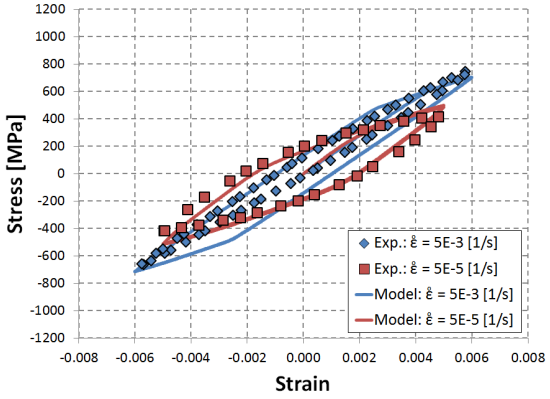

(b) 871°C.

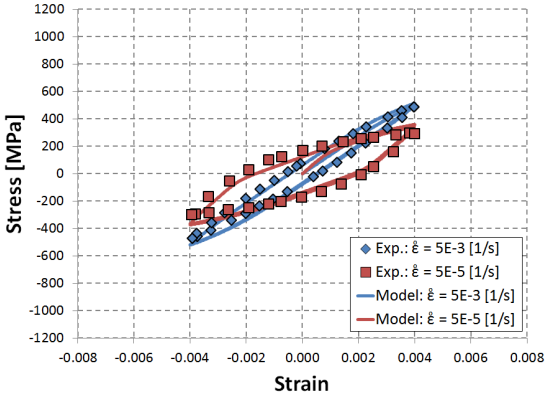

(c) 927°C.

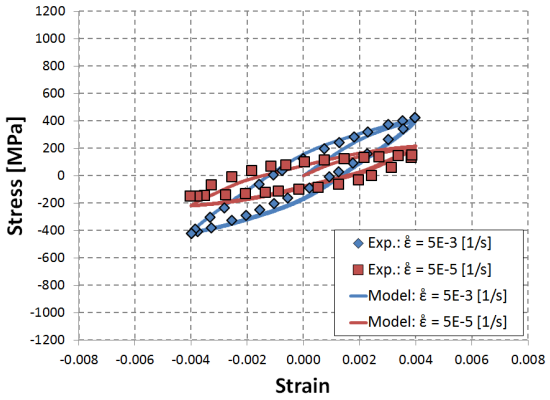

(d) 982°C.

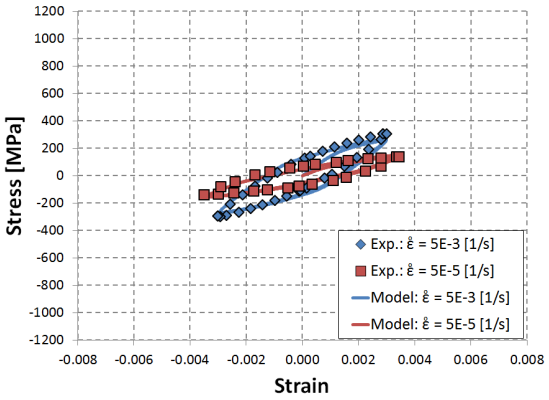

(e) 1038°C.

Figure 4.4: Isothermal fatigue experimental data and model predictions.

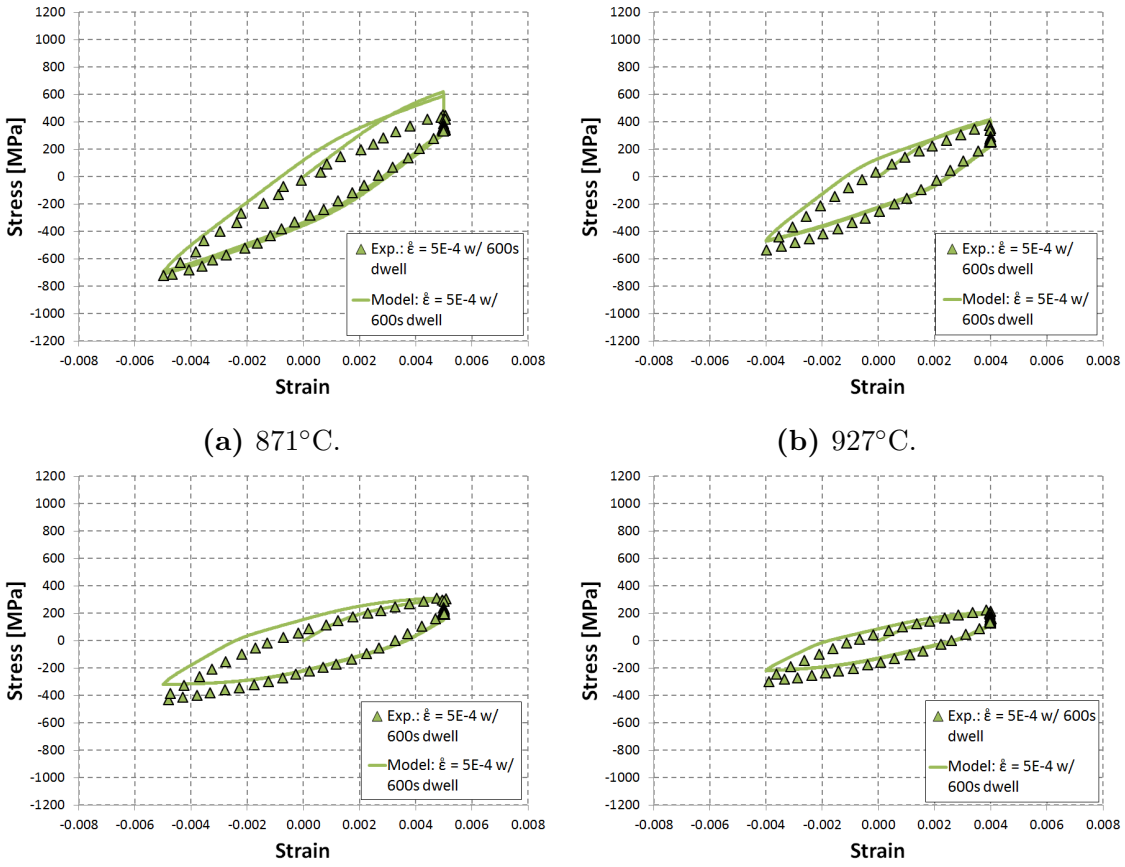

(a) 871°C. **(b)** 927°C.

(c) 982°C. **(d)** 1038°C.

Figure 4.5: Dwell experimental data and model predictions.

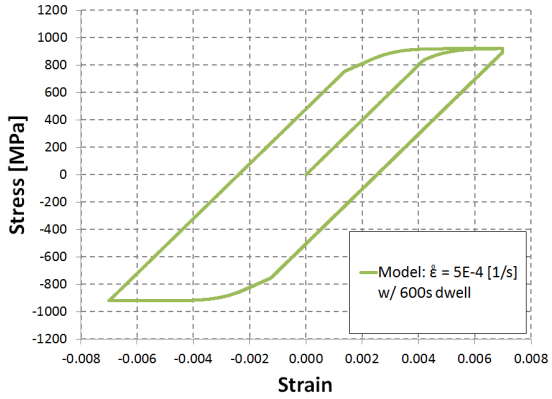

Figure 4.6: Dwell model prediction for 500°C.

4.4 Variability Due to Coarse-grained Microstructure

Nickel-based superalloys demonstrate large elastic anisotropies. For example, at room temperature the elasticity tensor components C_{11}, C_{12}, and C_{44} are equal to 258.6 GPa, 167.0 GPa, and 125.0 GPa, respectively [76]. This results in an anisotropy ratio, defined for cubic crystals as

$$A = \frac{2C_{44}}{(C_{11} - C_{12})} \tag{4.12}$$

equal to 2.7 where the elastic modulus has a minimum bound of 125.0 GPa and a maximum bound of 306.1 GPa. Due to the small number of crystallographic grains in the gage section of the test specimens and the large elastic anisotropy of the superalloy crystals, the measured elastic modulus varied widely among the different test specimens.

To better understand the variation observed, the theoretical bounding values of elastic modulus based on the extremum values of the extremes in single crystal orientation (minimum in the $\langle 001 \rangle$ direction and maximum in the $\langle 111 \rangle$ direction) are compared to the experimentally measured values. The theoretical bounding values for elastic modulus have been found using the temperature dependent elastic modulus values for single crystal Mar-M002, which is a Ni-based superalloy with similar composition to Mar-M247 [76]. A comparison of chemical compositions is shown in

Table 1.1. The comparison of the bounding elastic modulus and the observed elastic modulus of the test specimens is shown in Figure 4.7 for the specimens used in the isothermal fatigue tests. It can be seen that while the observed elastic moduli of the test specimens show a great deal of variation, they all fall within the limiting bounds computed from single crystal properties.

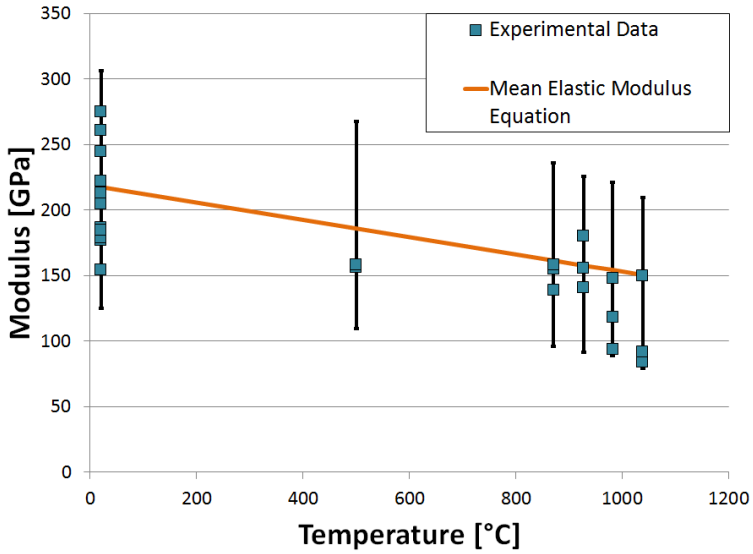

Figure 4.7: Variation in elastic modulus as a function of temperature. Equations shown in Table 4.4.

The constitutive model of this work is intended to model the homogenized and nominally isotropic behavior of a polycrystalline material. Even though Mar-M247 has highly anisotropic elastic properties, the material may be treated as isotropic if the number of randomly oriented grains is sufficient to average out the material response at the scale of interest. In the case of this work, the scale of interest corresponds to the cross-sectional area of the test specimens. The grain size of the material observed by Boismier and Sehitoglu was small enough to enable the material to be treated as isotropic [9].

It is clear from Figure 4.7, however, that the large grains observed in the specimens of this study require consideration of the elastic anisotropy in order to accurately

predict the elastic behavior. Such considerations would require microstructure modeling that is beyond the scope of this work, but the effects of the variation in elastic modulus on life predictions will be demonstrated in the life prediction section of this thesis.

For the current set of constitutive parameters, the variation in elastic modulus is not considered. The elastic modulus equation was fit to the mean value of the possible extremum values. This equation for the temperature dependence of elastic modulus follows the mean of the bounding modulus values to within 4.5%. The equations for elastic modulus may be found in Table 4.4.

The quality of the cyclic prediction can be significantly affected when the crystal orientation is well outside of the mean value (i.e., loading close to either $\langle 001 \rangle$ or $\langle 111 \rangle$ directions). For example, Figure 4.8a shows the prediction of an IF experiment using the mean elastic modulus. A prediction of this response using the measured elastic modulus is shown again in Figure 4.8b for comparison. In this case, the test specimen displayed a lower than average elastic modulus; therefore, the prediction over predicts the modulus in the elastic loading and unloading portions of the hysteresis loop. Clearly, accounting for this variation will impact life predictions since it affects the predicted amount of cyclic plastic strain.

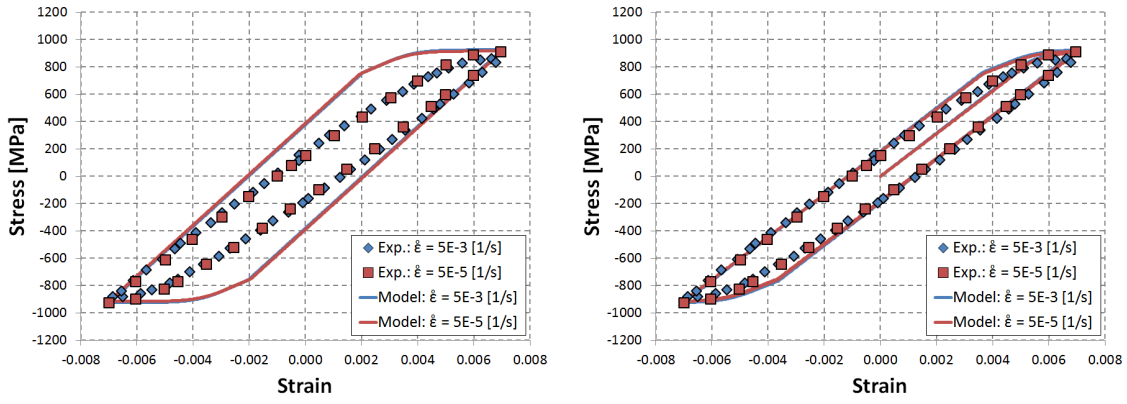

(a) Model prediction with mean modulus.

(b) Model prediction with experimental modulus.

Figure 4.8: Isothermal fatigue experimental data and model prediction at 500°C.

It was not a goal of this work to capture the variation in elastic modulus in the homogeneous constitutive model itself. For a test specimen or component with sufficiently small grains, the material may be homogenized and treated as isotropic, in which case the mean elastic modulus equation will closely match the material's elastic modulus for predicting the response of the test specimen or component.

The equations matching the upper and lower bounds of the bounding modulus predictions are shown below in Table 4.4. Also included is the equation used by Boismier-Sehitoglu, and the equation matching the mean value of the bounding values. The Boismier-Sehitoglu elastic modulus equation matches the predicted mean value equation to within 7% for temperatures between 500°C and 1038°C. For temperatures below 500°C, it is recommended that the predicted mean value equation or an equation matching a chosen data set be used. Figure 4.9 shows a comparison of the results of using the various elastic modulus equations.

Table 4.4: Elastic modulus equations. Temperatures in °C.

Eqn. Origin	**Equation**	**Units**
Boismier-Sehitoglu [9]	$E = 253900 - 107.8T$	[MPa]
Mar-M002 Predicted Mean	$E = 219069 - 66.0T$	[MPa]
Mar-M002 Predicted Max	$E = 310282 - 91.3T$	[MPa]
Mar-M002 Predicted Min	$E = 127856 - 40.8T$	[MPa]

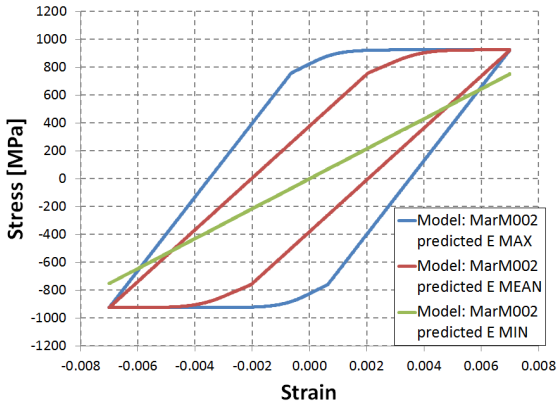

Figure 4.9: Comparison of modulus bounds predicted by Mar-M002 at a temperature of 500°C and strain rate of $5 \times 10^{-3} s^{-1}$.

4.5 TMF Verification

After calibrating the constitutive model with the isothermal and dwell experiments, the model was verified by comparing it to TMF experimental data. The TMF experiments included two out-of-phase and two in-phase tests. Each TMF test was thermally cycled between 500 and 1038°C while under mechanical strain loading and was performed at a mechanical strain rate of $3.33 \times 10^{-5} s^{-1}$.

The half-life data from the experiments are compared to the model prediction in Figures 4.10 and 4.11, where the legend entries correspond to the specimen IDs and associated test conditions shown in Table 3.3. In the model predictions, the simulation included as many cycles as the half-life of each corresponding test. For the two tests over large mechanical strain ranges shown in Figure 4.10, the model captures the stable hysteresis loop. These two tests reached stable hysteresis loops before the half-life, which was only 10 cycles in both cases.

For the two tests with smaller mechanical strain ranges shown in Figure 4.11, the model reasonably captures the stabilized hysteresis loop with the first cycle prediction, but in the remaining cycles, the model shows extensive ratcheting. The constitutive model is only intended to capture the stabilized hysteresis loop associated with saturated, non-evolving back stress hardening. This ratcheting behavior seen in the

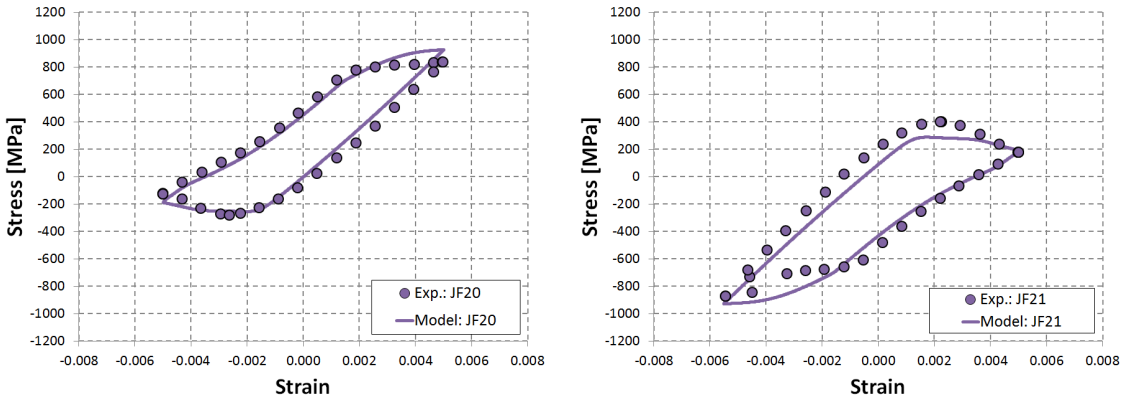

(a) OP TMF at 10 cycle half-life. **(b)** IP TMF at 10 cycle half-life.

Figure 4.10: TMF experimental data & model verification over a temperature range of 500–1038°C with a large strain range.

model, however, is caused by non-stabilized back stress evolution beyond the first cycle. This ratcheting behavior, then, demonstrates that care must be taken when using the constitutive model to predict TMF stress-strain behavior. While the first cycle prediction of the model captures the stabilized hysteresis loop well, there are cases when modeling additional cycles may cause the model to predict stress-strain responses different than that observed in the experimental response.

Proper use of the model is limited to this first cycle prediction of the stabilized hysteresis loop, and this is what was used when providing the life model with a stress-strain history. The reason the first cycle prediction is used is that the aim of the model is to be able to capture the stabilized response in a shorter analysis time, and therefore the first cycle prediction should capture the stabilized response.

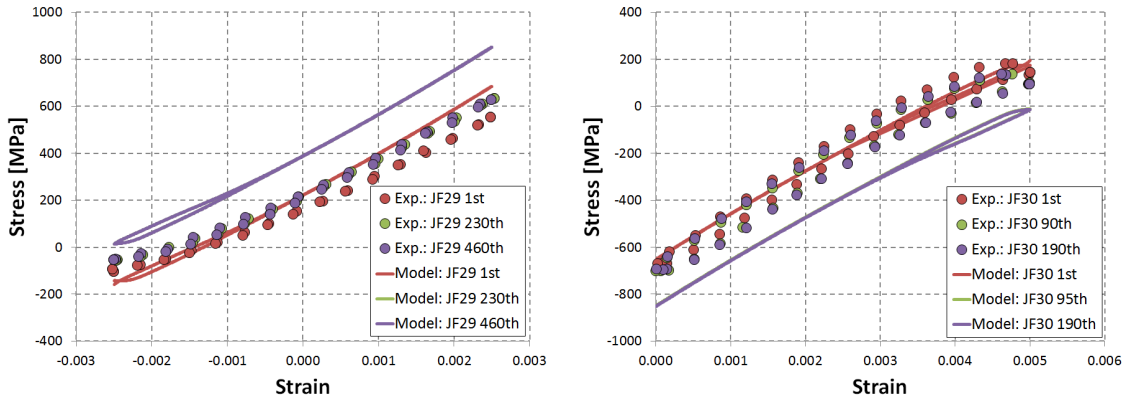

(a) OP TMF at 460 cycle half-life. **(b)** IP TMF at 190 cycle half-life.

Figure 4.11: TMF experimental data & model verification over a temperature range of 500–1038°C with a small strain range.

4.6 UMAT Implementation and Verification

To solve three-dimensional thermomechanical boundary value problems, the model was implemented as a User Material subroutine (UMAT) for the general purpose finite element code ABAQUS [77]. The fully three-dimensional UMAT was first written and verified for the 1070 steel model developed and calibrated by Slavik and Sehitoglu [48]. A fully implicit integration scheme was employed based on the method described in McGinty [78]. Once the implementation of the constitutive model was verified for the previously calibrated 1070 steel, it was updated with the new calibration and functional forms for Mar-M247 presented here and verified against the one-dimensional Matlab results, as shown in Figure 4.12.

Figure 4.13 shows an example 3-D thermomechanical boundary value problem. In this case, a disk is simulated using a quarter disk and symmetric displacement boundary conditions. A heat source is applied at the center of the disk, and the outer radius maintains a constant, minimum temperature. The resulting temperature profile varies from approximately 1038°C at the center to 500°C at the outer radius.

There was one significant difficulty encountered when verifying the UMAT implementation of the constitutive model. This difficulty was related to the expression used

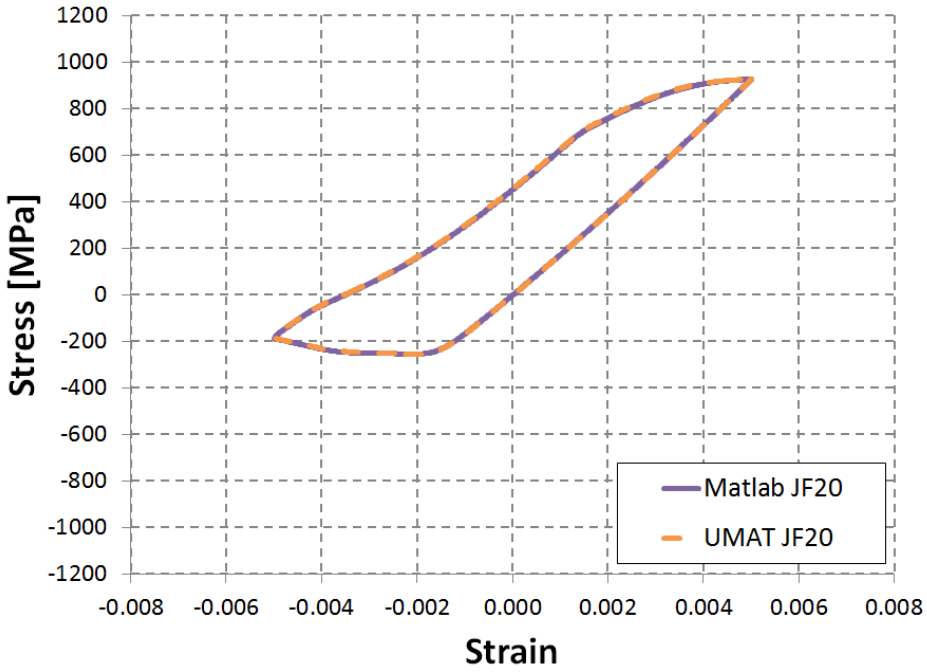

Figure 4.12: OP TMF comparison of UMAT and Matlab models.

for the coefficient of thermal expansion (CTE). The CTE used in the one-dimensional Matlab function was the same one given by Boismier and Sehitoglu [6],

$$CTE = \begin{cases} 1.57 \times 10^{-5} \ \frac{1}{^\circ C} & 500 < T \leq 685^\circ C \\ 2.05 \times 10^{-5} \ \frac{1}{^\circ C} & 685 < T \leq 1000^\circ C \end{cases} \tag{4.13}$$

In this work, the upper limit of the temperature range was taken to be 1038°C. This definition of CTE leads to a piecewise linear fit for the thermal strain curve when plotted against temperature.

When discretizing the time steps, this abrupt change in CTE across the temperature 685°C can cause problems in the TMF thermal strain calculation by artificially accumulating a thermal strain and developing a "drift" in the cyclic thermal strain. The simplest solution to the thermal drift problem is to use a constant value for the CTE. This solution was used in the UMAT implementation of the constitutive equation, where the constant value for the CTE was chosen as the value that would give the same thermal strain as the piecewise CTE over the temperature range of 500°C

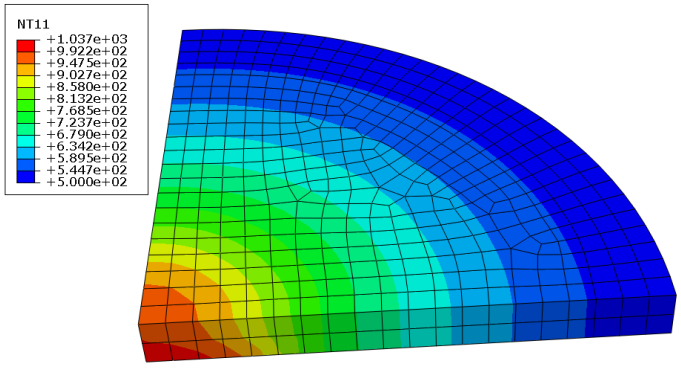

(a) Temperature contour plot [°C].

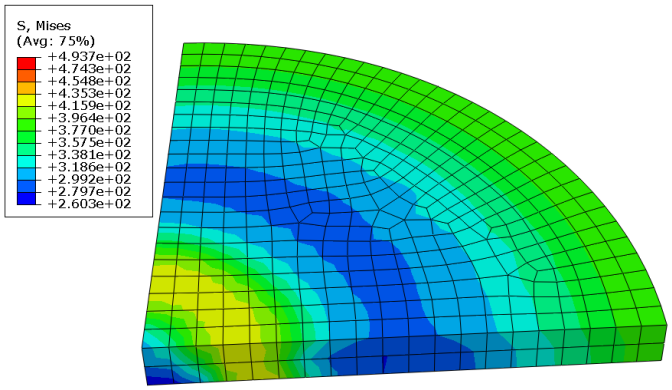

(b) Mises stress contour plot [MPa].

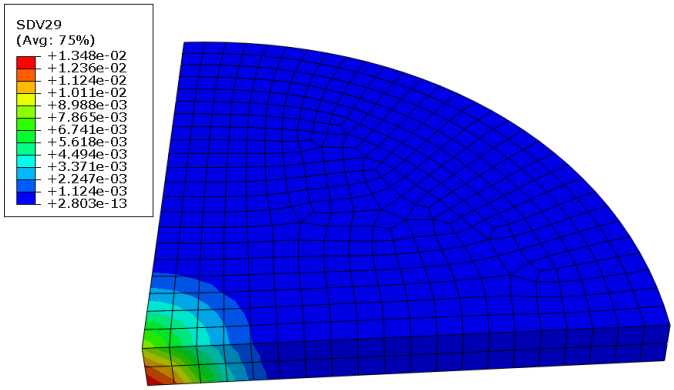

(c) Effective plastic strain contour plot [–].

Figure 4.13: 3-D thermomechanical boundary value problem.

to 1038°C. This solution provided results nearly identical to the one-dimensional implementation with a variable CTE. The constant value used for CTE can be found in Table 4.3.

One additional issue that may arise when running a UMAT implementation with

a TMF simulation is the sensitivity to time increment size. Problems arise in the UMAT when too large an increment size is used. Solutions for the implicit integration increments employed in the UMAT converge slowly for large increment sizes, and if the increment size is sufficiently large, it may be impossible to find a converged solution. As a general reference for TMF simulations, time increments that resulted in a temperature change of approximately 1.0-1.5°C per increment seem to be a good balance between minimizing the number of increments required and ensuring that the increment size is not too large.

When running the TMF simulations with the UMAT, it was found that there was a limiting value for minimum time step size, as well. Typically, the time step size when running an ABAQUS simulation must start out quite small in order to help the UMAT converge for the initial time steps. Time step sizes of less than 1.0×10^{-5} seconds, however, caused thermal strain drift to occur that looked similar to the drift caused by a variable CTE. It was determined that the cause of this was a variable passed to the UMAT from ABAQUS called "dtemp". This variable is a measure of the difference in temperature from the beginning to the end of a step. For very small time step values in TMF simulations, the dtemp variable was set equal to zero by ABAQUS, despite the fact that a non-negligible temperature change was being made across the time step. The solution to this problem was to use a larger initial time step size that would still be small enough to allow easy convergence for the initial steps in the UMAT. An initial time step size on the order of 1.0×10^{-4} or 1.0×10^{-3} seconds was found to fix the dtemp problem without causing convergence problems for the initial time steps.

CHAPTER V

TMF LIFE MODEL

5.1 Damage Mechanisms

The life model used in this work is based on the damage model developed by Neu and Sehitoglu for 1070 steel [49] [12], and used by Sehitoglu and Boismier for Mar-M247 [6] [9]. The damage model considers damage caused by fatigue, environment (oxidation), and creep. The total damage is the sum of the damage caused by fatigue, oxidation, and creep.

$$D^{tot} = D^{fat} + D^{env} + D^{creep} \tag{5.1}$$

If life is taken to be the inverse of damage, the equation may be written in terms of life as

$$\frac{1}{N_f^{tot}} = \frac{1}{N_f^{fat}} + \frac{1}{N_f^{env}} + \frac{1}{N_f^{creep}} \tag{5.2}$$

It was shown by Neu and Sehitoglu that in OP TMF loading, the environmental damage term dominates the total life prediction, while IP TMF loading life is dominated by the creep damage term. The fatigue damage term is expected to dominate only for isothermal loading at relatively low temperatures and high strain rates [12].

5.1.1 Fatigue Damage Term

The fatigue life term is represented by the power law strain-life equation,

$$\frac{\Delta\epsilon_{mech}}{2} = C\left(2N_f^{fat}\right)^d \tag{5.3}$$

This fatigue life relationship is the same one used by Boismier and Sehitoglu [9], but has been re-calibrated to the low temperature, high strain-rate data from this work. The fatigue life term is intended to capture the fatigue mechanisms which occur at

lower temperatures and higher strain rates under isothermal loading. The fatigue damage equation was calibrated to the life data at temperatures at or below 760°C. The calibration values of the constants may be found in Table 5.1.

Table 5.1: Fatigue life parameters.

C	**d**
[cycle^{-d}]	[–]
0.0105	-0.102

5.1.2 Environmental-Fatigue Interaction Damage Term

The environmental damage term is intended to capture damage caused by crack nucleation and growth due to oxidation and γ' depletion coupled with cyclic loading. Environmental damage is calculated by assuming that an environmentally induced crack is grown from zero to a critical length and then by integrating over the growth rate to find the number of cycles required to reach the critical crack length [9].

The crack growth rate with respect to cycles can be broken into two terms using the chain rule as,

$$\frac{dh}{dN} = \frac{dh}{dt} \cdot \frac{dt}{dN} \tag{5.4}$$

where h is the environmentally induced fatigue crack length and dt/dN is the cycle period [9]. A parabolic growth law can be used to represent oxidation and γ' depletion in Ni-based superalloys. Two effective parabolic constants, one for oxidation and one for γ' depletion are defined as,

$$K_{peff} = \frac{1}{t_c} \int_0^{t_c} D_0 exp\left(\frac{-Q}{RT(t)}\right) dt \tag{5.5}$$

where D_0 is the diffusion coefficient, Q is the activation energy, R is the universal gas constant, $T(t)$ is the temperature in kelvins which varies with time, and γ' is the period of the cycle [9]. Under repeated rupture of the oxidation layer and γ' depleted

layer, the oxidation growth is no longer parabolic but non-linear according to

$$h = \frac{B\left(K_{peff}^{ox} + K_{peff}^{\gamma'}\right)t^{\beta}}{\bar{h}_f} \tag{5.6}$$

where

$$\bar{h}_f = \frac{\delta_0}{\left(\Delta\epsilon_m\right)^2 \Phi^{env}\dot{\epsilon}^b} \tag{5.7}$$

is the average thickness of oxide and γ' depleted layer at rupture of the layer [9]. In equation 5.6, B is the constant coefficient and β is the constant exponent of the oxidation growth equation. In equation 5.7, δ_0 is a measure of the oxide and γ' depleted layer ductility, $\Delta\epsilon_m$ is the mechanical strain range, Φ^{env} is the environmental phasing factor, $\dot{\epsilon}$ is the mechanical strain rate, and b is the mechanical strain rate sensitivity [9].

The purpose of including a phasing factor is to differentiate between isothermal, in-phase, and out-of-phase loading conditions because the amount of damage will vary depending on the loading conditions. A phasing factor is a function of loading condition and will have values between zero and unity. A value of zero indicates that no damage is done under the current loading conditions, while a value of unity indicates that the full damage is done under the current loading conditions. In the case of environmental damage, the full amount of damage is expected under out-of-phase loading conditions, while no damage is expected under in-phase loading conditions. Values between zero and unity indicate partial amounts of damage at intermediate loading conditions. An example of an intermediate loading condition is when the temperature range is small with respect to the mechanical strain range so that the loading conditions approach isothermal conditions, or when the temperature range is very large with respect to the mechanical strain range so that the loading conditions approach free expansion or contraction.

The environmental phasing factor was changed in this work from that used by Boismier and Sehitoglu. The original phasing factor was a function of the ratio of

thermal strain rate to mechanical strain rate [9]. This strain rate ratio indicates the loading condition. If the strain rate ratio is equal to zero, then the thermal strain rate is zero and the material is under isothermal loading conditions. If the strain rate ratio is negative, then the thermal strain and mechanical strain are out-of-phase, and the material is under out-of-phase loading conditions. Conversely, if the strain rate ratio is positive, the material is under in-phase loading conditions. It was found that this form of the phasing factor was overly sensitive to the strain rate ratio due to the increased rate sensitivity at higher temperatures, and was adjusted in such a way to remove this sensitivity. The environmental phasing factor is taken as

$$\Phi^{env} = \left\langle \Phi_{iso}^{env} + \frac{1 - \Phi_{iso}^{env}}{1 + \left(\frac{\Delta T_0}{T_{max} - T_{min}}\right)^s} \cdot \frac{T\left(\epsilon_{mech,min}\right) - T\left(\epsilon_{mech,max}\right)}{T_{max} - T_{min}} \right\rangle \tag{5.8}$$

where Φ_{iso}^{env} is the phasing factor for isothermal conditions, ΔT_0 is a reference transition temperature range, and s is the sensitivity to temperature range. The $\langle\ \rangle$ symbols are MacCaulay brackets. The second factor in the product on the right hand side of the equation adjusts the phasing factor from positive to negative values as the history changes from out-of-phase loading to in-phase loading. In this form of the environmental phasing factor, emphasis is placed on the effects of temperature range instead of the strain rate.

This form of the environmental phasing factor offers less flexibility for arbitrary load histories; however, the original form did not allow a satisfactory calibration to the OP TMF experimental data. An example of the flexibility of the original equation can be seen when Boismier and Sehitoglu were able to accurately predict the life curve of a diamond shaped phasing in a thermomechanical load history [9]. In order to account for arbitrary phasing in load histories, the phasing factor must be a continuous function of the ratio of thermal strain rate to mechanical strain rate. Since the original equation could not be calibrated over the extended temperature range, the new form was chosen as a simple solution that allowed calibration for OP

TMF over a variety of temperature ranges. A more complex and adjustable form for the phase factor as a function of the strain rate ratio would be required in order to maintain the ability to predict life for arbitrary load histories. It is expected that such an equation would appear similar in shape to the original equation used by Boismier and Sehitoglu when plotted against the ratio of thermal strain rate to mechanical strain rate.

The environmental damage term is defined by differentiating equation 5.6 with respect to time and substituting the results into equation 5.4 and integrating,

$$\frac{1}{N_f^{env}} = \left[\frac{h_{cr}\delta_0}{B\Phi^{env}\left(K_{peff}^{ox} + K_{peff}^{\gamma'}\right)}\right]^{-1/\beta} \frac{2\left(\Delta\epsilon_m\right)^{(2/\beta)+1}}{\dot{\epsilon}^{1-(b/\beta)}} \tag{5.9}$$

where h_{cr} is the critical crack length for environmental damage trailing the crack tip [9]. Between the Boismier and Sehitoglu calibration and the calibration of this work, only the critical crack length value remained the same. The calibration of the environmental-fatigue damage term comes from oxidation tests. Calibration of the environmental phase factor was performed by comparing the relative changes in the fatigue lives of OP TMF specimens with different temperature ranges. The values of the calibration from this work are given in Table 5.2.

Table 5.2: Environmental life parameters.

Parameter	Value	Units
b	0.25	[–]
β	0.5	[–]
B	0.007	$[s^{(-\beta+1)}]$
δ_0	2.87×10^{-14}	$[\mu m \cdot s^{-b}]$
D_0^{ox}	0.0133	$[\mu m^2/s]$
Q_0^{ox}	81.8	$[kJ/mol]$
$D_0^{\gamma'}$	1.03×10^{-3}	$[\mu m^2/s]$
$Q_0^{\gamma'}$	49.4	$[kJ/mol]$
h_{cr}	461.4	$[\mu m]$
Φ_{iso}^{env}	0.1	[–]
ΔT_0	50	$[^\circ C]$
s	2	[–]
R	8.314×10^{-3}	$[kJ/K/mol]$

5.1.3 Creep Damage Term

The creep damage equation is taken to be

$$\frac{1}{N_f^{creep}} = \Phi^{creep} \int_0^{t_c} A^{creep} exp\left(\frac{-\Delta H}{RT}\right) \left(\frac{\alpha_1 \bar{\sigma} + \alpha_2 \sigma_H}{K}\right)^m dt \tag{5.10}$$

where Φ^{creep} is the creep damage phasing factor, A^{creep} is the creep damage coefficient and a material constant, m is the creep damage exponent and a material constant, ΔH is the activation energy for the creep mechanism, R is the universal gas constant, T is the temperature history given in kelvins, $\bar{\sigma}$ is the von Mises effective stress, σ_H is the hydrostatic stress, K is the saturated drag stress, and α_1 and α_2 are scaling factors controlling how much damage is done in tension versus compression in a uniaxial experiment [9]. In general, temperature, effective stress, hydrostatic stress, and drag stress are all functions of time. Since only the saturated drag stress is considered in this work, the drag stress is only a function of temperature. The exponential term inside the integral represents the Arrhenius type dependence on temperature of creep

damage. In the stress term inside the integral, the values of α_1 and α_2 are set so that in a uniaxial test, compression will not cause creep damage. In this work, only the values of α_1 and α_2 remain unchanged from the calibration of Boismier and Sehitoglu, although the activation energy was only changed slightly. The calibration of the creep damage parameters was made using IP TMF life data. The temperature dependent term was calibrated by comparing the relative changes in the fatigue lives of IP TMF specimens with different temperature ranges and the exponent m was calibrated by correlating the simulation life predictions to the experimental data. The creep damage parameter calibrations used in this work are given in Table 5.3.

It was necessary to change the form of the creep damage phasing factor in order to properly calibrate the creep damage term to the IP TMF experimental data. At a fixed strain rate and temperature range over the large range of mechanical strain amplitudes tested, the ratio of thermal strain rate to mechanical strain rate changes from near zero for large mechanical strain amplitudes to values around five or six for small mechanical strain amplitudes. The phasing factor used by Neu and Sehitoglu [12] for steel and again by Boismier and Sehitoglu [9] for Mar-M247 proved to be overly sensitive to the strain rate ratio, which caused the predicted life curve to be too flat to allow proper calibration of the creep damage function to the in-phase TMF data.

It was found that the proper calibration could be achieved more easily if the general shape of the original phasing factor was retained, but with added control over the slope of the function at either side of the peak value. This was achieved with two logistic functions summed in the same manner as the damage terms. In this way, the slope between isothermal conditions and the peak phasing factor could be controlled independently of the slope between the peak value and free expansion conditions. The form of the new phasing factor is taken as

$$\Phi^{creep} = \frac{1}{t_c} \int_0^{t_c} 2 \left[\frac{1}{\Psi_1} + \frac{1}{\Psi_2} \right]^{-1} dt \tag{5.11}$$

where

$$\Psi_1 = \frac{1}{1 + exp\left(-C_1\left(\frac{\dot{\epsilon}_{th}}{\dot{\epsilon}_{mech}}\right) - D_1\right)} \tag{5.12}$$

$$\Psi_2 = \frac{(1-y)}{1 + exp\left(-C_2\left(\frac{\dot{\epsilon}_{th}}{\dot{\epsilon}_{mech}}\right) - D_2\right)} + y \tag{5.13}$$

In equation 5.11, Φ^{creep} is the creep damage phasing factor, and t_c is the period of the cycle. The multiplier of two is required to make the maximum phase factor equal to one. Equations 5.12 and 5.13 describe the two logistic functions used to control the slope of the phasing factor function. In these equations, the values of C_1 and C_2 control the slope of the logistic functions, the values of D_1 and D_2 control the location of strain rate ratio where the logistic function reaches the median value, and the value of y controls a shift of the second logistic function along the y axis accompanied by an appropriate modification of the height of the logistic function, which is determined by the numerator.

The shape of the new creep phasing factor is shown in Figure 5.1. As discussed with the environmental phase factor, the purpose of the creep phase factor is to distinguish between loading conditions and adjust the amount of creep damage appropriately. More creep damage is expected under in-phase loading conditions, while no creep damage is expected under out-of-phase loading conditions. Note that a zero strain rate ratio corresponds to isothermal loading, a positive strain rate ratio corresponds to in-phase loading, a negative strain rate ratio corresponds to out-of-phase loading, and very large absolute values of strain rate ratio indicate that the loading conditions are approaching free expansion or contraction.

Although this new phasing factor does not tend toward zero as the load history tends towards free expansion, it should be noted that the stress term will decrease towards zero as free expansion is reached, so the creep damage will decrease naturally in this way. It should also be noted that at the smallest mechanical strain ranges in the temperature range of 500 to 1038°C, the strain rate ratio is already very

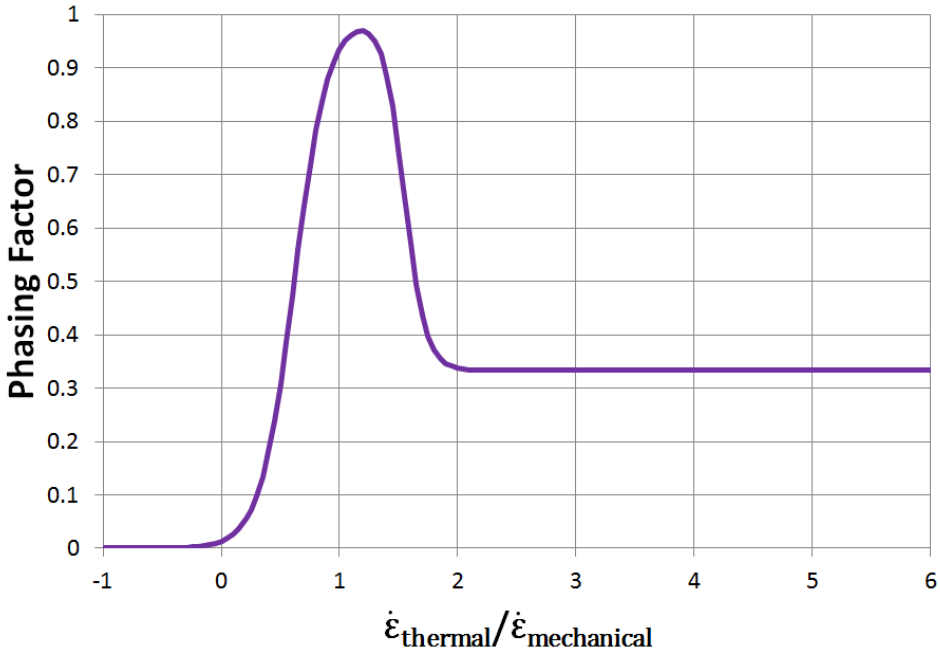

Figure 5.1: Creep phasing factor.

close to what was considered free expansion in the work by Neu and Sehitoglu [12]. The experimental life data for this strain range and temperature range, however, corresponds to life under IP TMF load history. This justifies the extension of a non-zero creep phasing factor in the direction of free expansion. The creep phasing factor was calibrated such that non-negligible creep damage would be predicted for these larger strain rate ratios. The slope of the creep phasing factor were calibrated by considering the relative changes in fatigue lives of the experimental data over different temperature ranges. This new phase factor allowed the satisfactory calibration of the creep damage term to the IP TMF experimental data without changing the form of the creep damage equation, although a small decrease in the activation energy of the temperature term was made to improve the overall calibration. The creep phasing factor parameters used for the calibration are given in Table 5.3.

Table 5.3: Creep life parameters.

Parameter	Value	Units
A^{creep}	8.0×10^{22}	$[1/s]$
m	8.7575	[–]
ΔH	500.0	$[kJ/mol]$
R	8.314×10^{-3}	$[kJ/K/mol]$
α_1	1/3	[–]
α_2	1	[–]
C_1	7	[–]
D_1	0.715	[–]
C_2	-11	[–]
D_2	1.5	[–]
y	0.2	[–]

5.2 Life Correlations

The constitutive model is calibrated from 500 to 1038°C, but some TMF experimental life data included tests with a minimum temperature as low as 427°C. In order to be able to make life predictions under the same TMF load history, some assumptions had to be made in order to use the constitutive model below 500°C. In this work, for temperatures less than 500°C, it is assumed that the hardening parameters take the same values as they do at 500°C and that the flow rule calibration holds. The previous assumption of a constant coefficient of thermal expansion is maintained, as well. It has already been shown in Figure 4.7 that the mean elastic modulus equation of Table 4.4 captures the elastic modulus as a function of temperature from room temperature up to 1038°C.

The constitutive model calibration and verification experiments also provided data for calibrating the life model. Before presenting the full set of total life model predictions, it is important to understand the general trends of damage interaction under the four types of loading presented in the constitutive modeling sections.

5.2.1 Damage Term Interactions

The phase factors of the environmental-fatigue damage and creep damage were calibrated such that the TMF life predictions would be dominated by environmental damage under out-of-phase conditions and by creep damage under in-phase conditions. This is consistent with the damage mechanisms expected to dominate life under the two extremes of TMF loading conditions, and the effects can be seen in the damage interaction plots shown in Figures 5.2 and 5.3. This is the same approach originally used by Neu and Sehitoglu [12] and followed by Boismier and Sehitoglu [9].

As an example of the interaction of the damage terms under OP TMF loading, consider the model prediction of OP TMF between the temperatures of 427 to 927°C at a fixed cycle time of 60 seconds shown in Figure 5.2. For the OP TMF case, so little creep damage is predicted that the creep life prediction is very large and the creep life curve does not fit on the axes of the plot.

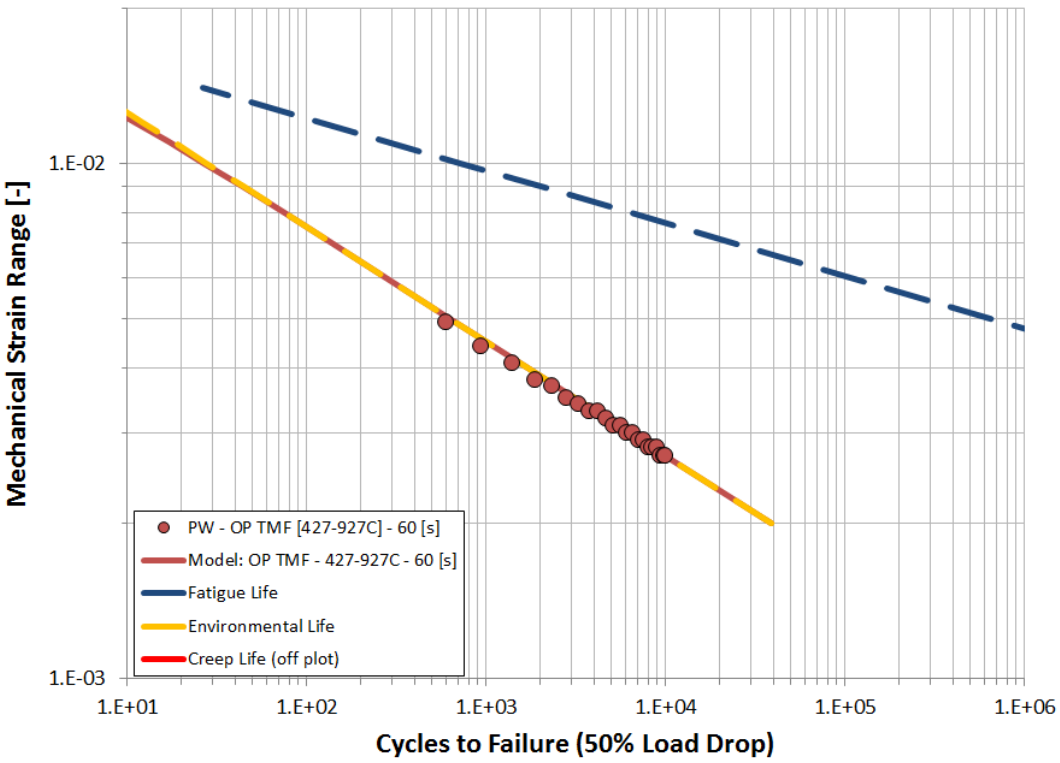

Figure 5.2: Damage interaction for OP TMF at 427-927°C with fixed 60 second cycle time.

Figure 5.3 is an example of the interaction between damage terms under IP TMF loading for a case with a temperature range between 427 and 982°C at a fixed cycle time of 60 seconds. In the case of IP TMF loading, the environmental life curve cannot be seen because the environmental damage is predicted to be very small, and the corresponding environmental life to be very large.

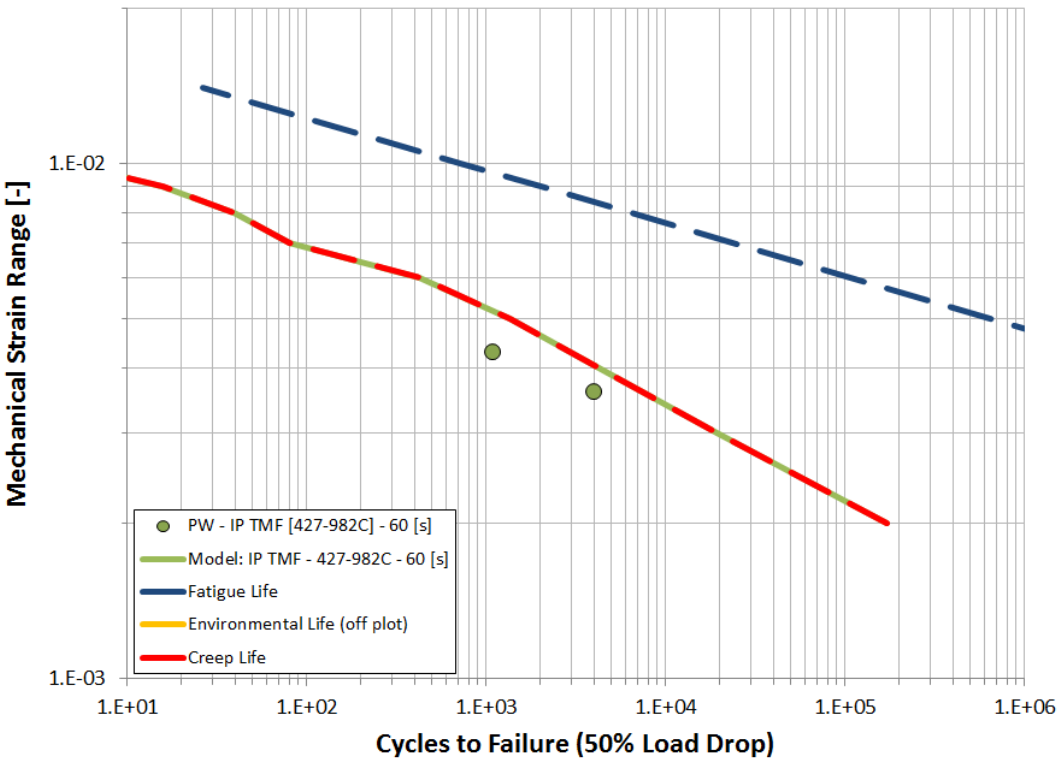

Figure 5.3: Damage interaction for IP TMF at 427-982°C with fixed 60 second cycle time.

Under isothermal fatigue at low temperatures and high strain rates, the experimental data was fit with a power law strain life curve. Under isothermal loading at higher temperatures and lower strain rates, the total life is not expected to be dominated by any particular damage mechanism, but rather to be a combination of all three damage mechanisms. A typical case for damage interaction at the relatively high temperature of 927°C under isothermal loading can be seen in Figure 5.4. It is typical of the higher temperature isothermal life predictions to show similar damage term interactions as seen in Figure 5.4. This interaction starts at 871°C for slower strain rates and is seen in all of the higher temperatures for all strain rates.

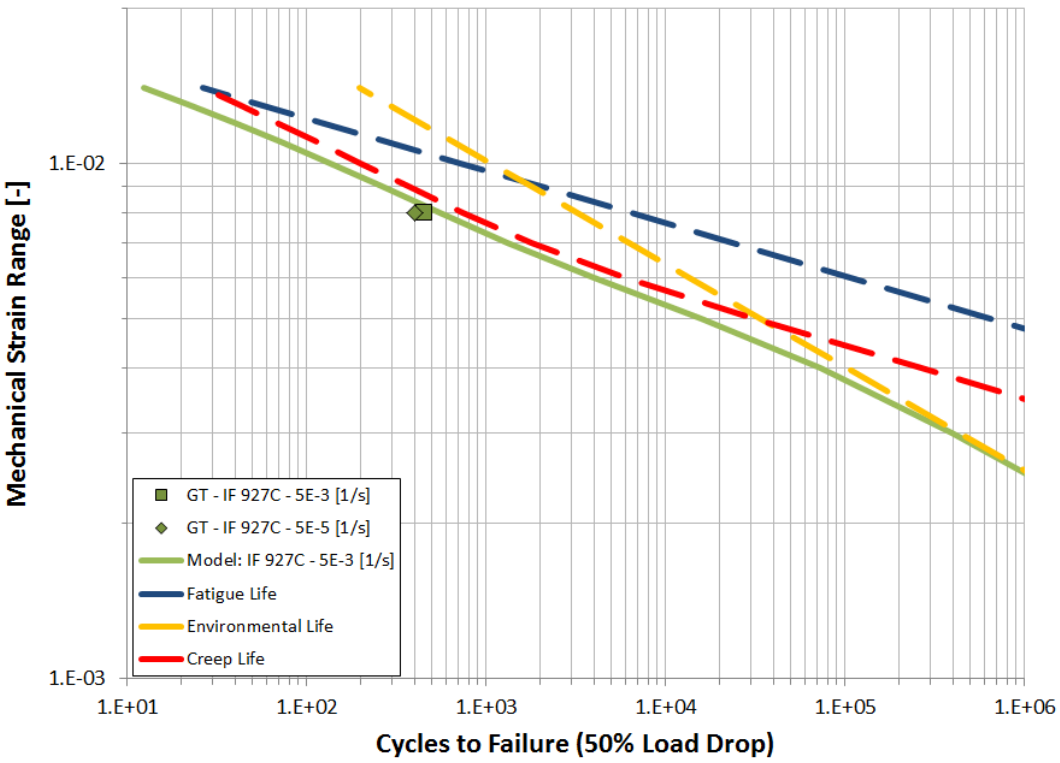

Figure 5.4: Damage interaction at 927°C under isothermal loading with a strain rate of $5.0 \times 10^{-3} s^{-1}$.

For the dwell tests, the creep and environmental damage terms are expected to interact due to the higher temperatures, relatively low strain rate, and long holds at maximum strain. This interaction can be seen in Figure 5.5 for a dwell test at a temperature of 871°C.

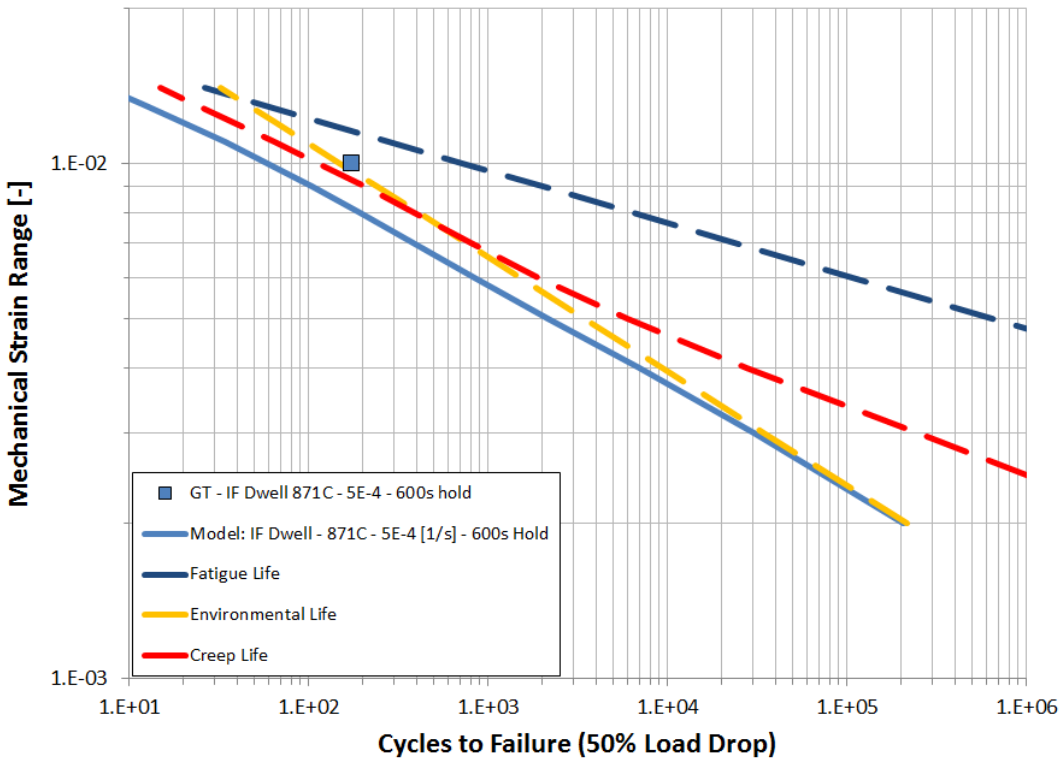

Figure 5.5: Damage interaction at 871°C under isothermal loading with dwells at a strain rate of $5.0 \times 10^{-4} s^{-1}$.

5.2.2 Life Plots

The total life prediction curves for different test conditions are shown in Figures 5.6–5.8. The effects of various damage interactions can be discerned by considering the slope of the total life curve and the load history. The fatigue life term is entirely empirical and does not change with changing temperature history or changing TMF load types such as OP and IP loading. In general, the environmental life term has the steepest slope of the three terms, and the slope does not change much over the full range of load histories. The environmental life term appears linear on a log-log plot. The creep life term typically has an intermediate slope in comparison to the other two life terms, and is not strictly linear on a log-log plot.

Between the environmental term and the creep term, the creep term tends to dominate at higher strain ranges and the environmental term tends to dominate at

the lower strain ranges. Some non-linearity in the plots is caused by the interaction of the damage terms, but the creep term also introduces some non-linearity at the higher strain ranges, especially under IP TMF.

It should be noted that three rate control types were used in the experimental data and the corresponding life predictions shown in the plots: mechanical strain rate control with units of strain per second, cycle frequency control with units of cycles per minute, and cycle period control with units of seconds per cycle. In the life plots, the rate control type is denoted by the units in the legend.

First, the life predictions under low temperature IF are presented in Figure 5.6a. In the low temperature IF life prediction plot, life predictions at temperatures equal to or below 500°C are identical to the empirical fatigue life term. For this reason, there is not a separate life prediction curve plotted at 27°C. The effects of environmental term on the total life prediction can be seen to start interacting with the fatigue term at temperatures as low as 760°C. At 871°C, especially at the slower strain rate, the creep term can be seen interacting with the total life prediction at high strain ranges, while the environmental term is still present for the lower strain ranges.

Since the 500°C and 760°C life predictions use different rate control types, it is informative to compare a 500°C life prediction using cycle frequency rate control to the life prediction of the 760°C case. It was found that changing the rate control type at 500°C from mechanical strain rate control at $5 \times 10^{-3} s^{-1}$ to cycle frequency rate control at 10 cpm made no appreciable difference to the 500°C life prediction, which is shown in Figure 5.6a. However, changing the 760°C life prediction to mechanical strain rate control at $5 \times 10^{-3} s^{-1}$ did increase the predicted life below 0.5% mechanical strain range. The result is shown in Figure 5.6a.

The life predictions for higher temperatures under isothermal fatigue are shown in Figure 5.6b. At higher temperatures, the creep and environmental terms clearly dominate the total life prediction for all strain rates.

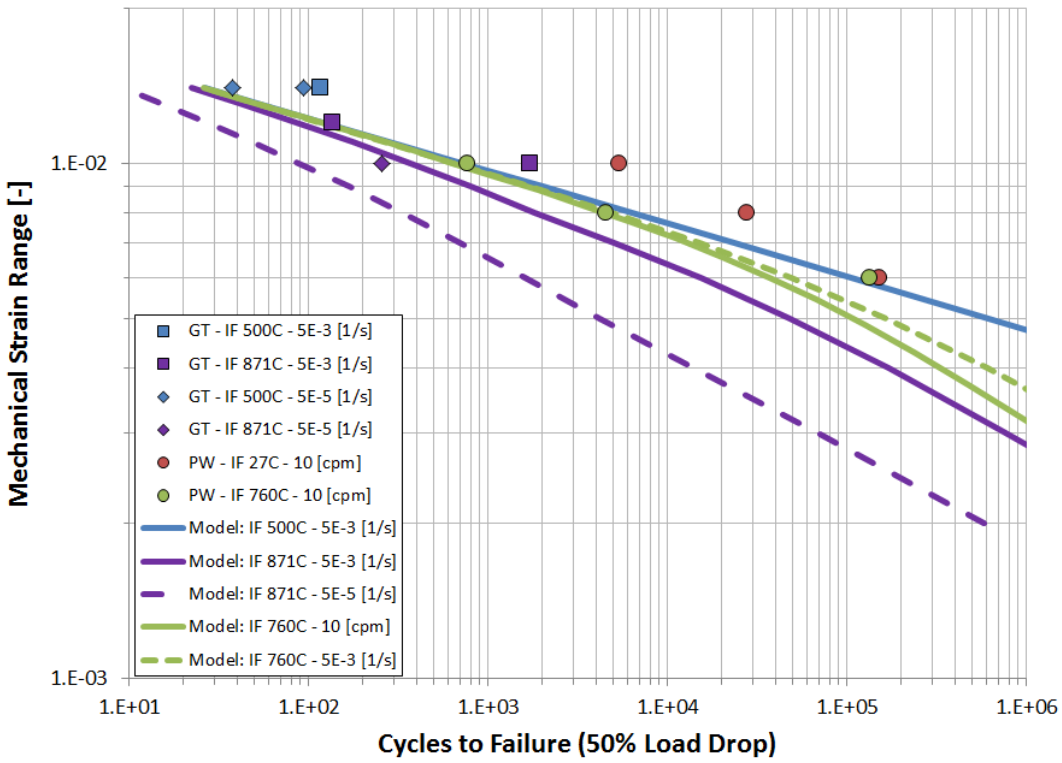

(a) Low temperature.

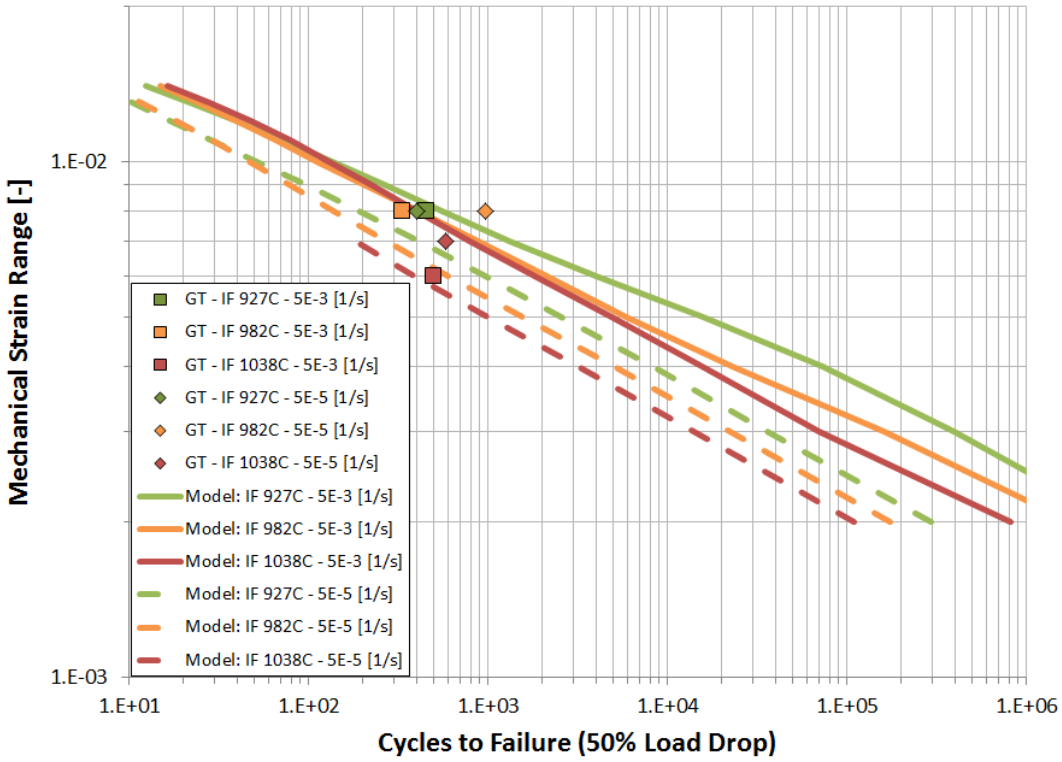

(b) High temperature.

Figure 5.6: Isothermal fatigue life predictions and experimental life data.

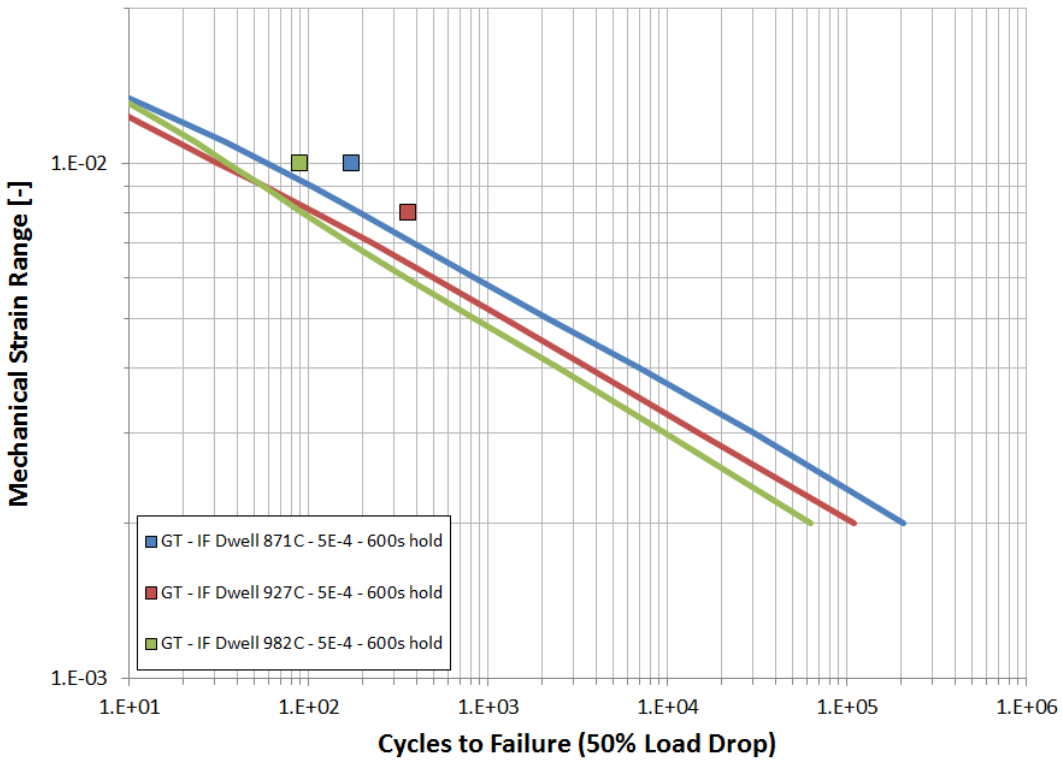

Figure 5.7: Dwell life predictions and experimental life data.

The dwell predictions are compared against the dwell tests in Figure 5.7. In the comparison of the dwell predictions to the experimental data, both the creep and environmental terms contribute to the total life prediction. The creep term is more significant at higher strain ranges, while the environmental term dominates at the lower strain ranges. The dwell life predictions are based on the calibrations of the life model under IP and OP TMF loading. Consequently, the conservative prediction of the model in comparison to the dwell life data arises from the conservative prediction of life seen at the higher strain ranges under these loading conditions, which is discussed in the next section on IP and OP TMF life prediction.

Figure 5.8a shows the total life predictions under OP TMF loading. As previously discussed, the environmental damage term dominates the life prediction under OP TMF loading conditions.

The IP TMF life predictions are compared to experimental life data in Figure 5.8b.

As noted previously, the creep damage term dominates the life prediction under IP TMF loading conditions. The non-linearity of the creep term can be clearly seen in the plot of IP TMF life predictions. It proved difficult to calibrate the creep damage model due to the wide array of temperatures considered under TMF loading. The behavior of the damage terms for the smaller temperature range of 500-871°C and the larger temperature range of 500-1038°C was sufficiently different that calibrating the creep damage model for both required careful adjustments to the calibration of the phase factor in conjunction with calibration adjustments of the damage parameters. The predictions shown represent the overall best calibration to the data shown using the current form for creep damage.

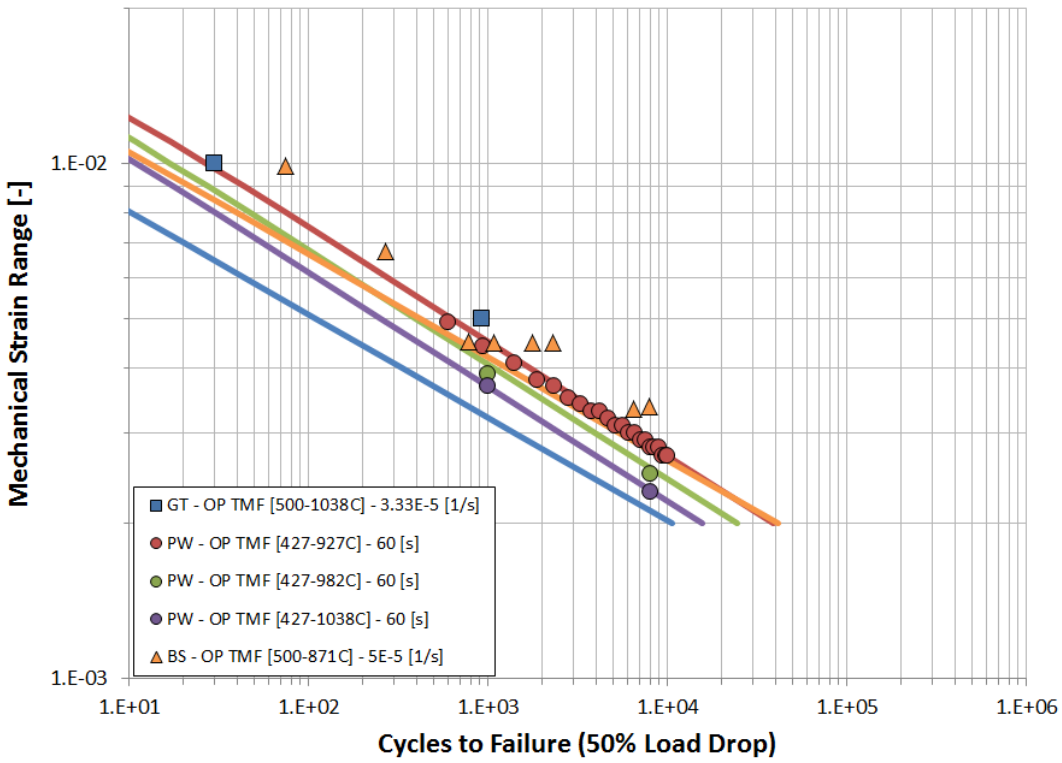

(a) OP TMF.

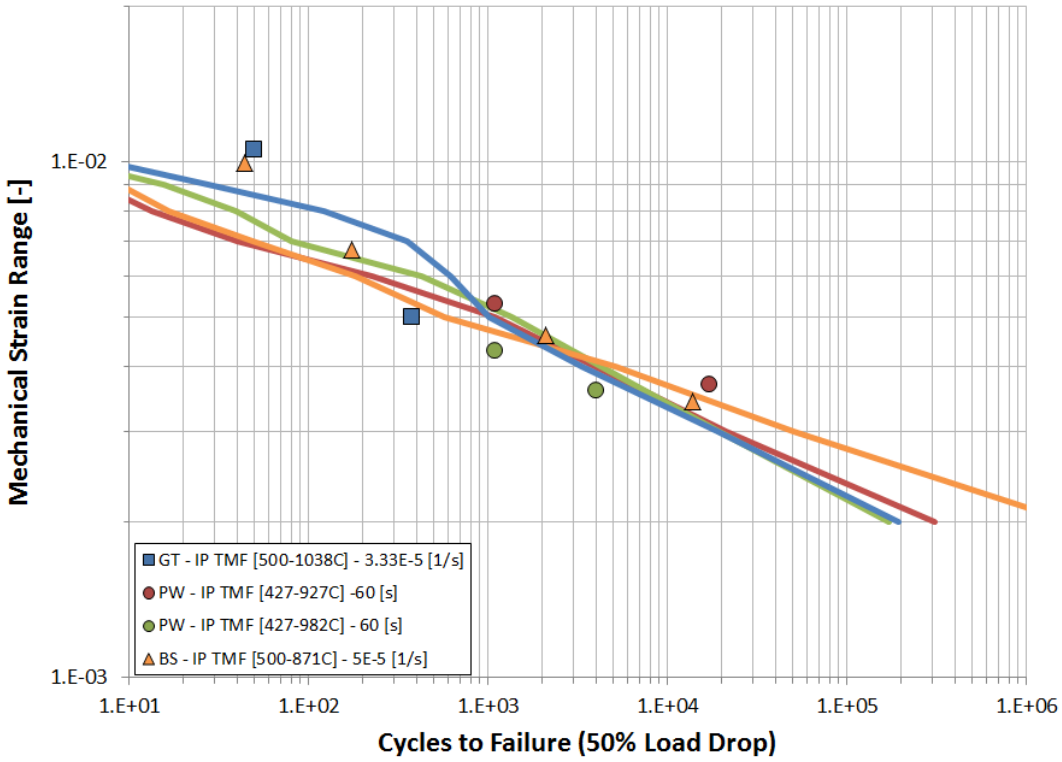

(b) IP TMF.

Figure 5.8: TMF life predictions and experimental life data.

As a final exercise in life prediction, the effects of elastic modulus variability on predicted total life were modeled. Since the creep damage term is the only term that depends on the stress predictions of the constitutive model, the creep life prediction is the only life term that is affected by this change. Consequently, OP TMF life predictions will not be affected, but IP TMF and high temperature, slow strain rate IF loading will be affected. Following this observation, and noting that a lower modulus corresponds to lower stresses as seen in Figure 4.9, it is expected that a lower modulus will increase the creep life, while a higher modulus will decrease the creep life.

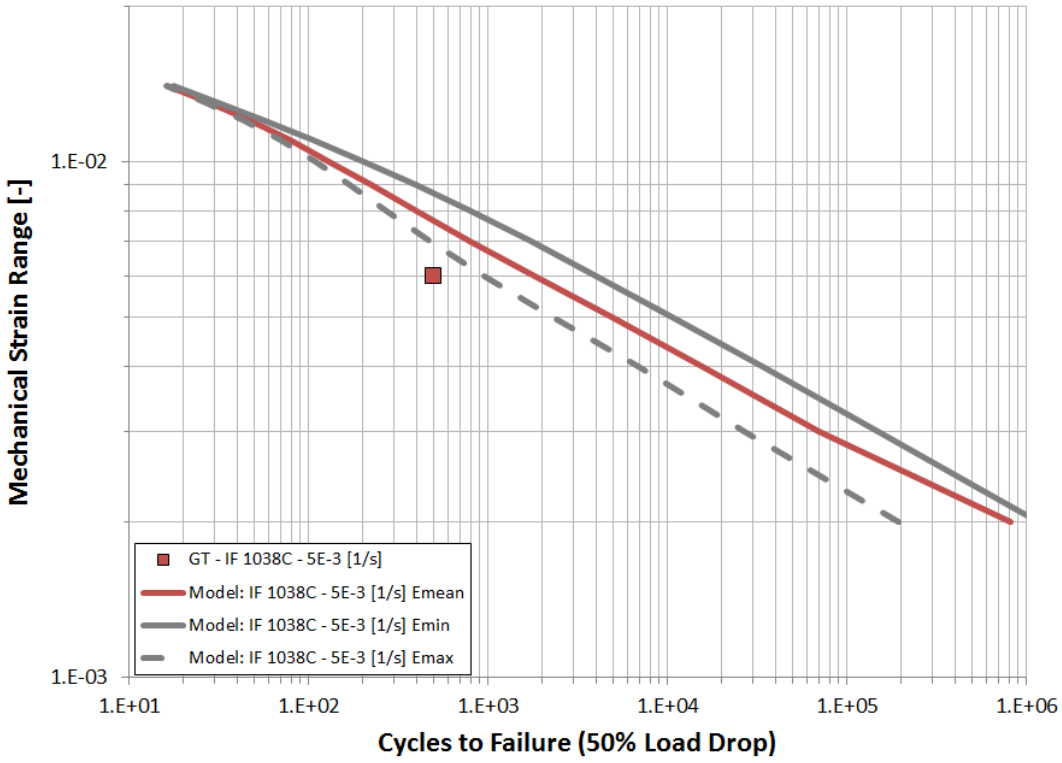

Figure 5.9: Predicted variability in total life as a function of extremes in possible modulus values.

Figure 5.9 shows the changes in total life caused by using the minimum and maximum modulus values in comparison to the original prediction using the mean modulus value for the case of IF loading at 1038°C and $5.0 \times 10^{-3} s^{-1}$ strain rate. As

expected, a lower elastic modulus increases the life, while a larger elastic modulus decreases the life. In the case presented in this figure, the three total life predictions converge at high strain ranges where environmental and fatigue life, which remain unchanged, dominate the total life prediction.

CHAPTER VI

CONCLUSIONS

The thermo-viscoplastic constitutive equation represents the behavior of the polycrystalline Ni-base superalloy Mar-M247 over an extended temperature range from 500°C to 1038°C. The rate sensitivity, temperature sensitivity, and stress relaxation in a strain hold are adequately captured using parameters determined from isothermal cyclic inelastic strain experiments with and without dwells. The extension to higher temperatures and the inclusion of dwells required a lower stress exponent in the power law factor of the flow rule. The model successfully predicts out-of-phase and in-phase thermomechanical cycles.

The crystallographic grain size of the specimens used in the calibration was large in comparison to the gage section resulting in a large variability in the measured cyclic stress-strain response. The influence of coarse grains is primarily tied to the limits on the elastic properties estimated from a crystal elasticity analysis. Using the elastic properties of a single-crystal superalloy of similar chemical composition, the extent of the variation in the elastic response is captured. The model implementation as a UMAT for the general purpose finite element solver ABAQUS enables the solving of simulations involving thermomechanical boundary values.

Using the calibrated constitutive model, life predictions were made for four different load histories: isothermal fatigue, isothermal fatigue with dwells, out-of-phase thermomechanical fatigue, and in-phase thermomechanical fatigue. The life model uses three different damage models to predict a variety of different damage mechanisms that may be found under the differing load histories. The life prediction model

successfully predicts differences in the life curves under differing load histories. Extending the life model to a higher temperature range required a form change in the phasing factors for both the environmental and creep damage models as well as a recalibration for most of the constants used in the damage models. The effects on life prediction caused by the large grains and resultant variation in the elastic modulus have been demonstrated.

Reviewing the specific research objectives presented in Section 1.3, the work presented addresses the following:

1. The unified constitutive model was extended to a maximum temperature of 1038°C and captures the stable stress-strain response of both isothermal and thermomechanical load histories including creep and stress-relaxation while accounting for the effects of strain rate.

2. The unified constitutive model was validated using both in-phase and out-of-phase thermomechanical fatigue tests.

3. The life model was calibrated and accounts for fatigue, creep and environmental-fatigue damage under both isothermal and thermomechanical load histories.

CHAPTER VII

RECOMMENDATIONS

There are several areas where this research could be extended and improved. Presented below are three recommendations for further work.

One of the largest challenges in calibrating the constitutive model was the large temperature range under consideration. It may be possible to improve upon the calibration of the constitutive model with a new flow rule formulation. Possible changes include using a flow rule which includes a temperature dependent term to help account for changing mechanisms over the large temperature range. It is anticipated that such a term would be formulated following an Arrhenius type relationship involving an activation energy for higher temperatures around 871°C. An example of the use of such a temperature dependent term can be found in an article by Shenoy et al. [79].

Another challenge presented by the large temperature range under consideration was the calibration of the phase factors for the environmental-fatigue and creep damage terms of the life model. A form for the creep phase factor was established that retained the flexibility to handle arbitrary load histories; however, a similar solution for the environmental-fatigue phase factor proved difficult to calibrate. Accordingly, a simpler environmental phase factor was used. In order for the life model to account for arbitrary load histories, the life model would require an environmental phase factor based on the ratio of thermal strain rate to mechanical strain rate with a shape similar to the original environmental phase factor used by Boismier and Sehitoglu. It's anticipated that such a phase factor would require a formulation similar to that used by the creep phase factor in this work. In order to fully validate the ability of

the phase factors to handle arbitrary load histories, TMF tests with load histories other than in-phase or out-of-phase would need to be performed. Following Boismier and Sehitoglu, a diamond wave form would be an appropriate choice to validate the phase factors in the life model.

The final recommendation for further work pertains to the variability in the elastic modulus caused by the large grained microstructure. As previously discussed, large grains make the isotropic assumption inaccurate because the material behavior may no longer be homogenized across grains. In order to improve the constitutive model's prediction of the stress-strain history, the model must be able to account for the microstructure of the material. Such microstructural modeling is computationally expensive and would increase in complexity over the current model. Microstructural modeling would also require large simulations of multiple grains forming a representative volume element of the observed microstructure in a finite element analysis. A good reference for a similar analysis can be found in the work of McGinty [78]. The life model may only be improved with a suitable method for predicting the variability in elastic modulus. A microstructure sensitive constitutive model would allow greater fidelity in the life model by more accurately predicting the changes to the stress-strain history caused by an anisotropic elasticity tensor and the coarse grained microstructure. Such an analysis would introduce a great deal more complexity to the model than was intended by this work.

REFERENCES

[1] Pineau, A. and Antolovich, S. D., "High temperature fatigue of nickel-base superalloys - a review with special emphasis on deformation modes and oxidation," *Engineering Failure Analysis*, vol. 16(8), pp. 2668–2697, 2010.

[2] Reed, R. C., *The Superalloys: Fundamentals and Applications*. Cambridge University Press, 2008.

[3] U.S. Department of Energy, "How gas turbine power plants work." `http://energy.gov/fe/how-gas-turbine-power-plants-work`, October 2013.

[4] Rahimian, M., Milenkovic, S., and Sabirov, I., "Microstructure and hardness evolution in mar-m247 nni-based superalloy processed by controlled cooling and double heat treatment," *Journal of Alloys and Compounds*, vol. 550, pp. 339–344, 2013.

[5] Bor, H. Y., Wei, C. N., Jeng, R. R., and Ko, P. Y., "Elucidating the effects of solution and double ageing treatment on the mechanical properties and toughness of mar-m247 superalloy at high temperature," *Materials Chemistry and Physics*, vol. 109, pp. 334–341, 2008.

[6] Boismier, D. A. and Sehitoglu, H., "Thermo-mechanical fatigue of mar-m247: Part 1—experiments," *Journal of Engineering Materials and Technology*, vol. 112, pp. 68–79, January 1990.

[7] Suresh, S., *Fatigue of Materials*. Cambridge University Press, 2 ed., 1998.

[8] Milligan, W. W., "Yielding and deformation behavior of the single crystal superalloy pwa 1480," Master's thesis, Georgia Institute of Technology, March 1986.

[9] Sehitoglu, H. and Boismier, D. A., "Thermo-mechanical fatigue of mar-m247: Part 2—life prediction," *Journal of Engineering Materials and Technology*, vol. 112, pp. 80–89, January 1990.

[10] Sehitoglu, H., "Thermal and thermomechanical fatigue of structural alloys," *ASM Handbook.*, vol. 19, pp. 527–556, 1996.

[11] Sehitoglu, H., "Thermo-mechanical fatigue life prediction methods," in *Advances in Fatigue Lifetime Predictive Techniques* (Mitchell, M. R. and Landgraf, R. W., eds.), (Philadelphia), pp. 47–76, American Society for Testing and Materials, 1992.

[12] Neu, R. W. and Sehitoglu, H., "Thermo-mechanical fatigue, oxidation and creep part ii: A life prediction model," *Metallurgical Trans.*, vol. 20A, pp. 1769–1783, September 1989.

[13] Sehitoglu, H. and Karasek, M., "Observations of material behavior under isothermal and thermo-mechanical loading," *ASME Journal of Engineering Materials and Technology*, vol. 108, pp. 192–198, 1986.

[14] Sehitoglu, H., "Crack growth studies under selected temperature strain histories," *Engineering Fracture Mechanics*, vol. 26, pp. 475–489, 1987.

[15] Sehitoglu, H., "Constraint effects in thermo-mechanical fatigue," *Journal of Engineering Materials and Technology*, vol. 108, pp. 221–226, 1985.

[16] Jaske, C. E., "Thermal-mechanical, low-cycle fatigue of aisi 1010 steel," in *Thermal Fatigue of Materials and Components* (Spera, D. A. and Mowbray, D. F., eds.), no. ASTM STP 612, pp. 170–198, American Society for Testing and Materials, 1976.

[17] Sheffler, K. D., "Vacuum thermal-mechanical fatigue behavior of two iron-base alloys," in *Thermal Fatigue of Materials and Components* (Spera, D. A. and Mowbray, D. F., eds.), no. ASTM STP 612, pp. 214–226, American Society for Testing and Materials, 1976.

[18] Karasek, M. L., "An investigation into isothermal and thermomechanical fatigue damage at elevated temperatures," Tech. Rep. Report No. 132, Materials Engineering-Mechanical Behavior, College of Engineering, University of Illinois at Urbana-Champaign, August 1986.

[19] Nelson, R. S., Schoendorf, J. F., and Lin, L. S., "Creep fatigue life prediction for engine hot section materials (isotropic) interim report," Tech. Rep. Contractor Report 179550, NASA, December 1986.

[20] Majumdar, S., "Thermomechanical fatigue of type 304 stainless steel," *ASME PVP*, vol. 123, pp. 31–36, 1987.

[21] Halford, G. R., *Low-Cycle Thermal Fatigue*. Elsevier Science Publishers, 1987. Chapter 6, Thermal Stresses II.

[22] Neal, S., "Reduced order constitutive modeling of a directionally-solidified nickel-base superalloy," Master's thesis, Georgia Institute of Technology, May 2013.

[23] Amaro, R. L., *Thermomechanical Fatigue Crack Formation In A Single Crystal Ni-base Superalloy*. PhD thesis, Georgia Institute of Technology, December 2010.

[24] Fernandez-Zelaia, P., "Thermomechanical fatigue crack formation in nickel-base superalloys at notches," Master's thesis, Georgia Institute of Technology, August 2012.

[25] Gordon, A. P., *Crack Initiation Modeling of a Directionally-solidified Nickel-base Superalloy*. PhD thesis, Georgia Institute of Mechanical Engineering, May 2006.

[26] McDowell, D. L., Antolovich, S., and T., O. R. L., "Mechanistic considerations for tmf life prediction of nickel-base superalloys," *Nuclear Engineering and Design*, vol. 133, pp. 383–399, 1992.

[27] Das, D. K., Singh, V., and Joshi, S. V., "High temperature oxidation behaviour of directionally solidified nickel base superalloy cm-247lc," *Materials Science and Technology*, vol. 19, pp. 695–708, June 2003.

[28] Frost, H. J. and F., A. M., *Deformation-Mechanism Maps: The Plasticity and Creep of Metals and Ceramics*. Pergamon Press, 1982.

[29] Okada, M., Tsutsumi, M., T., K., and R., O., "Initiation and growth of small crack in directionally solidified mar-m247 under creep-fatigue. part i: Effect of microstructure," *Fatigue & Fracture of Engineering Materials & Structures*, vol. 21, pp. 741–750, 1998.

[30] Raj, R. and Ashby, M. F., "Intergranular fracture at elevated temperatures," *Acta Metallurgica*, vol. 23, p. 653, 1975.

[31] Baik, S. and Raj, R., "Wedge type creep damage in low cycle fatigue," *Metallurgical Transactions, A*, vol. 13A, pp. 1207–1214, 1982.

[32] Majumdar, S. and Maiya, P. S., "A mechanistic model for time-dependent fatigue," *ASME Journal of Engineering Materials and Technology*, vol. 102, pp. 159–167, 1980.

[33] Wareing, J., "Creep-fatigue interaction in austenitic stainless steels," *Metallurgical Transactions, A*, vol. 8A, pp. 711–721, May 1977.

[34] Jaske, C. E., "Creep-fatigue crack growth in type 316 stainless steel," in *ASME International Conference on Advances in Life Prediction Methods*, pp. 93–103, 1983.

[35] Grandt, Alten F., J., *Fundamentals of Structural Integrity: Damage Tolerant Design and Nondestructive Evaluation*. John Wiley and Sons, Inc., 2004.

[36] Valerio, P., Gao, M., and Wei, R. P., "Environmental enhancement of creep crack growth in inconel 718 by oxygen and water vapor," *Scripta Metallurgica et Materialia*, vol. 30, no. 10, pp. 1269–1274, 1994.

[37] Srinivas, S., Pandey, M. C., and Taplin, D. M. R., "Air-environment-creep interaction in a nickel base superalloy," *Engineering Failure Analysis*, vol. 2, no. 3, pp. 191–196, 1995.

[38] Evans, H. E. and Taylor, M. P., "Creep relaxation and the spallation of oxide layers," *Surface and Coatings Technology*, vol. 94-95, pp. 27–33, 1997.

[39] Kupkovits, R. A. and Neu, R. W., "Thermomechanical fatigue of a directionally solidified ni-base superalloy: Smooth and cylindrically-notched specimens," *International Journal of Fatigue*, vol. 32, p. 12, 2010.

[40] Evans, H. E., "Modelling oxide spallation," *Materials Under High Temperature*, vol. 12, no. 2-3, pp. 219–227, 1994.

[41] Nicholls, J., Evans, H. E., and Saunders, R. J., "Fracture and spallation of oxides," *Materials at High Temperatures*, vol. 14, no. 1, pp. 5–13, 1996.

[42] Wright, P. K., "Oxidation-fatigue interactions in a single-crystal superalloy," in *Low Cycle Fatigue* (et al., H. D. S., ed.), no. ASTM STP 942, (Philadelphia), pp. 558–575, American Society for Testing and Materials, 1988.

[43] Malpertu, J. L. and Rémy, L., "Influence of test parameters on the thermalmechanical fatigue behavior of a superalloy," *Metallurgical Transactions, A*, vol. 21, no. 2, pp. 389–399, 1990.

[44] Rémy, L., Bernard, H., Malpertu, J. L., and Rezai-Aria, F., "Fatigue life prediction under thermal-mechanical loading in a nickel-base superalloy," in *Thermomechanical Fatigue Behaviour of Materials* (Sehitoglu, H., ed.), no. ASTM STP 1186, (Philadelphia, PA), pp. 3–16, American Society for Testing and Materials, 1993.

[45] Vasseur, E. and Rémy, L., "High temperature low cycle fatigue and thermalmechanical fatigue behaviour of an oxide-dispersion-strengthened nickel-base superalloy," *Materials Science and Engineering A*, vol. 184, no. 1, pp. 1–5, 1994.

[46] Kowalewski, R. and Mughrabi, H., "Thermo-mechanical and isothermal fatigue of a coated columnar-grained directionally solidified nickel-base superalloy," in *The Symposium of Thermo-Mechanical Fatigue Behavior of Materials*, (Norfolk, VA), pp. 3–17, American Society for Testing and Materials, 2000.

[47] Slavik, D. and Sehitoglu, H., "A constitutive model for high temperature loading part i–experimentally based forms of the equations," in *Thermal Stress, Material Deformation, and Thermo-Mechanical Fatigue*, pp. 65–73, American Society of Mechanical Engineers, 1987.

[48] Slavik, D. and Sehitoglu, H., "A constitutive model for high temperature loading part ii–comparison of simulations with experiments," in *Thermal Stress, Material Deformation, and Thermo-Mechanical Fatigue*, pp. 75–82, American Society of Mechanical Engineers, 1987.

[49] Neu, R. W. and Sehitoglu, H., "Thermo-mechanical fatigue, oxidation and creep part i: A study of damage mechanisms," *Metallurgical Trans.*, vol. 20A, pp. 1755–1767, September 1989.

[50] Pugh, C. E. and Robinson, D. N., "Some trends in constitutive equation model development for high-temperature behavior of fast-reactor structural alloys," *Nuclear Engineering and Design*, vol. 47, pp. 269–276, 1978.

[51] Walker, K. P., "Research and development program for non-linear structural modeling with advanced time-temperature dependent constitutive relationships," Tech. Rep. PWA-5700-S0, United Technologies Research Center, 1981. (Also NASA CR-165533).

[52] "Nonlinear constitutive relations for high temperature applications–1984," in *NASA Conference Publication 2369*, June 1984.

[53] Mroz, Z., "Mathematical model of inelastic material behavior." University of Waterloo, Solid Mechanics Division, 1973.

[54] Drucker, D. C. and Palgen, L., "On stress-strain relations suitable for cyclic and other loading," *Journal of Applied Mechanics*, vol. 48, pp. 479–485, 1981.

[55] Cook, T. S., Kim, K. S., and McKnight, R. L., "Thermal mechanical fatigue of cast rene '80," in *ASTM Symposium on Low Cycle Fatigue*, (New York), October 1985.

[56] Krieg, R. D., "A practical two surface plasticity theory," *Journal of Applied Mechanics*, vol. 42, pp. 641–646, September 1975.

[57] Lambda, H. S., "Nonproportional cyclic plasticity," Tech. Rep. TAM report No. 413, Deptartment of Theoretical and Applied Mechanics, University of Illinois at U-C, 1976.

[58] Garud, Y. S., "A new approach to the evaluation of fatigue under multiaxial loadings," *Journal of Engineering Materials and Technology*, vol. 103, pp. 118–125, April 1981.

[59] McDowell, D. L., "A two-surface model for transient nonproportional cyclic plasticity: Part i–development of appropriate equations," *ASME Journal of Applied Mechanics*, vol. 52, pp. 298–308, June 1985.

[60] McDowell, D. L., "A two-surface model for transient nonproportional cyclic plasticity: Part ii–comparison of theory with experiments," *ASME Journal of Applied Mechanics*, vol. 52, pp. 298–308, June 1985.

[61] Bodner, S. R. and Partom, Y., "Constitutive equations for elastic-viscoplastic strain hardening materials," *Journal of Applied Mechanics*, vol. 42, pp. 385–389, 1975.

[62] Bodner, S. R., Partom, I., and Partom, Y., "Uniaxial cyclic loading of elastic-viscoplastic materials," *Journal of Applied Mechanics*, vol. 46, pp. 805–810, 1975.

[63] Bodner, S. R. and A., M., "Viscoplastic constitutive equations for copper with strain rate history and temperature effects," *Journal of Engineering Materials and Technology*, vol. 100, pp. 388–394, 1978.

[64] Miller, A., "An inelastic constitutive model for monotonic, cyclic, and creep deformation: Part i and part ii," *Journal of Engineering Materials and Technology*, vol. 98, pp. 97–113, April 1976.

[65] Hart, E. W., "Constitutive relations for nonelastic deformation of metals," *Journal of Engineering Materials and Technology*, vol. 98, pp. 193–202, 1976.

[66] Ponter, A. R. S. and Leckie, F. A., "Constitutive relationships for the time-dependent deformation of metals," *Journal of Engineering Materials and Technology*, vol. 98, pp. 47–51, January 1976.

[67] Abrahamson, T. E., *Modeling the Behavior of Type 304 Stainless Steel with a Unified Creep-Plasticity Theory*. PhD thesis, University of Illinois at U-C, 1983.

[68] Slavik, D. C. and Sehitoglu, H., "Constitutive models suitable for thermal loading," *Journal of Engineering Materials and Technology*, vol. 108, pp. 303–312, 1986.

[69] Coffin, L. F., J., "Fatigue at high temperature," in *Fatigue at Elevated Temperatures*, no. ASTM STP 520, pp. 5–34, American Society for Testing and Materials, 1973.

[70] Challenger, K. D., Miller, A. K., and Langdon, R. L., "Elevated-temperature fatigue with hold time in a low-alloy steel: a predictive correlation," *J. Materials for Energy Systems*, vol. 3, pp. 51–61, June 1981.

[71] Antolovich, S. D., Baur, R., and Liu, S., "A mechanistically based model for high-temperature lcf of nickel-base superalloys," in *Superalloys 1980*, pp. 605–613, American Society for Metals, September 1980.

[72] Antolovich, S. D., Liu, S., and Baur, R., "Low-cycle fatigue behavior of rene 80 at elevated temperature," *Metallurgical Transactions, A*, vol. 12A, pp. 473–481, 1981.

[73] Halford, G. R. and Manson, S. S., "Life prediction of thermal-mechanical fatigue using strainrange partitioning," in *Thermal Fatigue of Materials and Components* (Spera, D. and Mowbray, D., eds.), no. ASTM STP 612, pp. 239–254, American Society for Testing and Materials, 1976.

[74] Chaboche, J. L.: in, *Engineering Approaches to High Temperature Design*, vol. 2. Pineridge Press, 1983.

[75] Slavik, D. and Cook, T. S., "A unified constitutive model for superalloys," *International Journal of Plasticity*, vol. 6, pp. 651–664, 1990.

[76] Kuhn, H. A. and Sockel, H. G., "Comparison between experimental determination and calculation of elastic properties of nickel-base superalloys between 25 and 1200 deg. c," *Phys. Status Solidi (a)*, vol. 110, pp. 449–458, December 1988.

[77] Dassault Systemes, "Abaqus v. 6.11-1. 2011." Providence, RI, USA.

[78] McGinty, R. D., *Multiscale Representation of Polycrystalline Inelasticity*. PhD thesis, Georgia Institute of Technology, 2001.

[79] Shenoy, M. M., Gordon, A. P., McDowell, D. L., and Neu, R. W., "Thermomechanical fatigue behavior of a directionally solidified ni-base superalloy," *Journal of Engineering Materials and Technology*, vol. 127, pp. 325–336, July 2005.